Supplementary Information

Modulation of *d-d* orbital hybridization via creating asymmetrical paired iron sites for oxygen reduction reaction

Zhijun Li[1,*], Hongxue Liu[1], Yunlu Chen[4], Siqi Ji[1,*], Xue Lu[1], Wenkai Yang[1], Yu Wang[4], J. Hugh Horton[5], Yu-Jia Tang[3,*], Xinlong Tian[2,*]

[1] State Key Laboratory of Continental Shale Oil, Joint International Research Laboratory of Advanced Chemical Catalytic Materials & Surface Science, College of Chemistry and Chemical Engineering, Northeast Petroleum University, Daqing 163318, P. R. China

[2] State Key Laboratory of Tropic Ocean Engineering Materials and Materials Evaluation, School of Materials Science and Engineering, Hainan Provincial Key Lab of Fine Chem, Hainan University, Haikou 570228, P. R. China

[3] School of Chemistry and Materials Science, Nanjing University of Information Science & Technology, Nanjing 210044, P. R. China

[4] Jiangsu Collaborative Innovation Centre of Biomedical Functional Materials, School of Chemistry and Materials Science, Nanjing Normal University, Nanjing 210023, PR China

[5] Department of Chemistry, Queen′s University, Kingston, K7L 3N6, Canada

*Correspondence to: zhijun.li@queensu.ca; siqi.ji@nepu.edu.cn; tangyujia@nuist.edu.cn; tianxl@hainanu.edu.cn

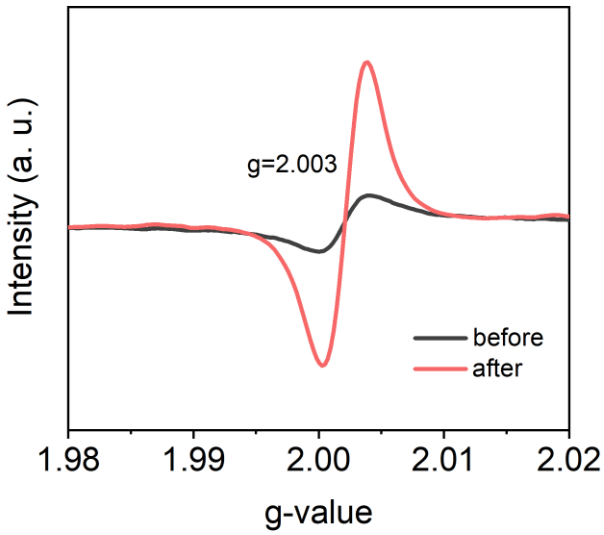

Fig. S1. EPR results of Fe_1/NCP before and after CO_2 activation.

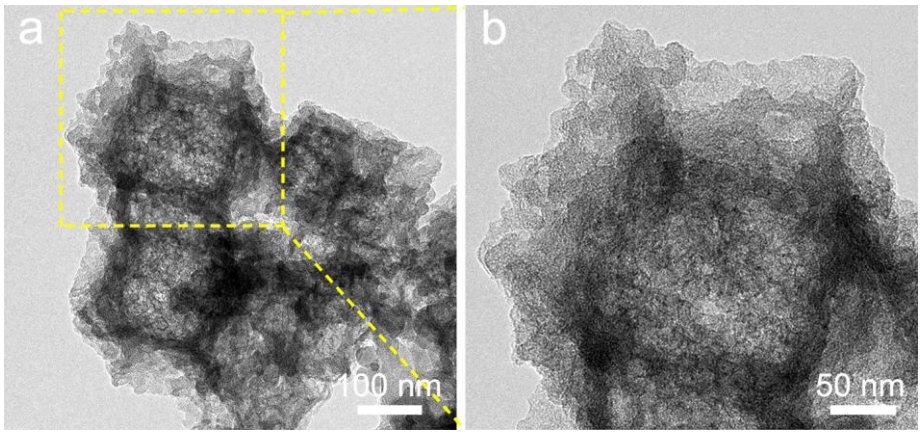

Fig. S2. (a) TEM image and (b) the corresponding enlarged image of Fe_2/NCP.

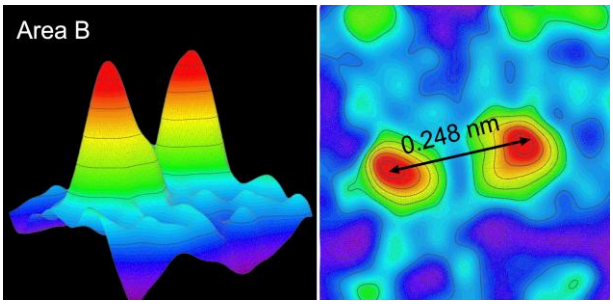

Fig. S3. Three-dimensional atom over-lapping Gaussian-function fitting maps of the atom pairs highlighted in the green box B in Fig. 1g.

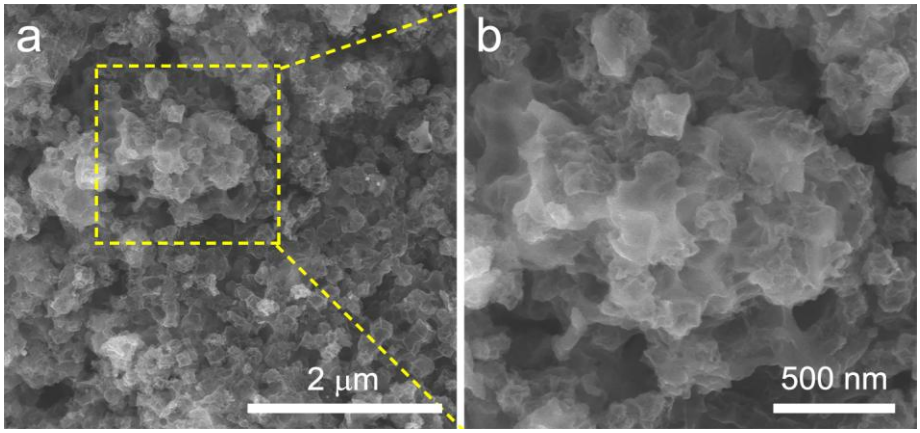

Fig. S4. (a) SEM image and (b) the corresponding enlarged image of Fe_2/NC.

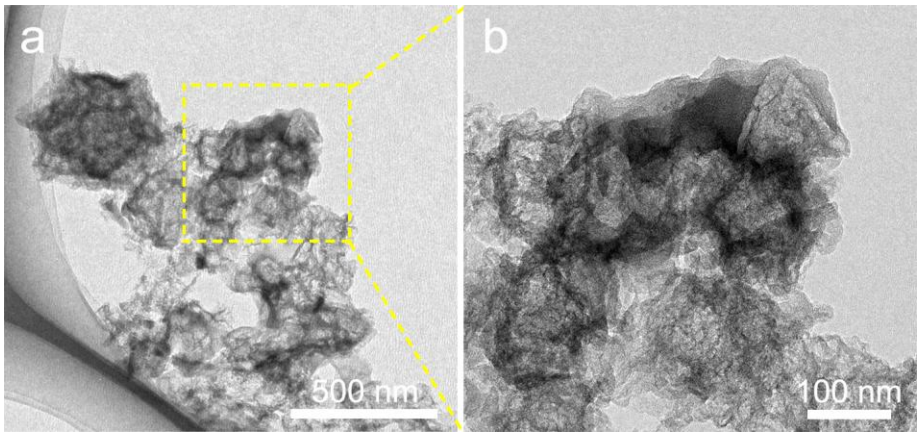

Fig. S5. (a) TEM image and (b) the corresponding enlarged image of Fe_2/NC.

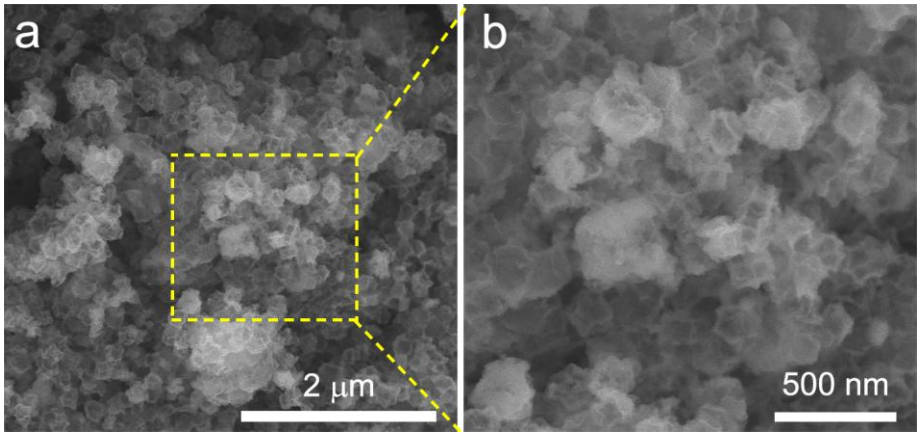

Fig. S6. (a) SEM image and (b) the corresponding enlarged image of Fe_1/NC.

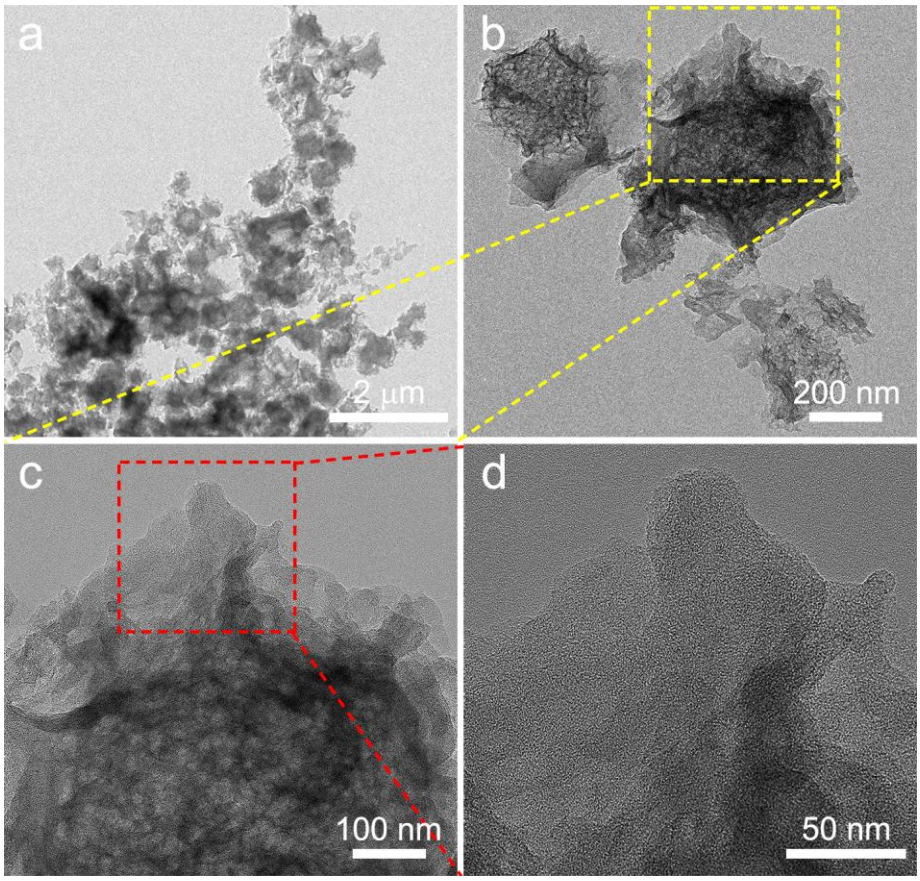

Fig. S7. (a,b) TEM images and (c,d) the corresponding enlarged images of Fe_1/NC.

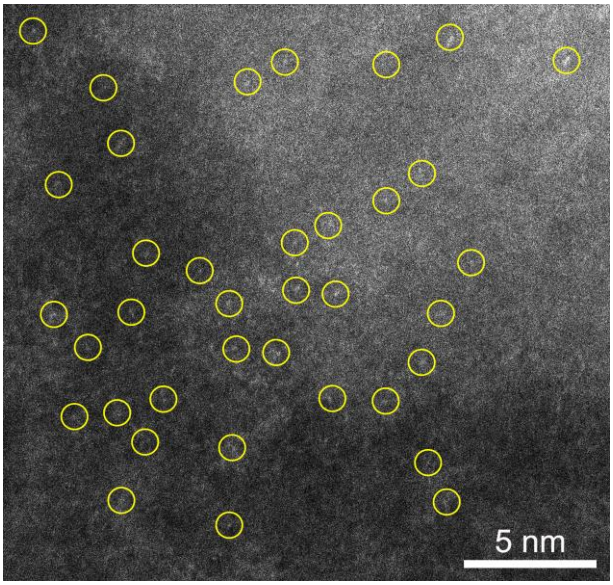

Fig. S8. AC HAADF-STEM image of Fe_1/NC.

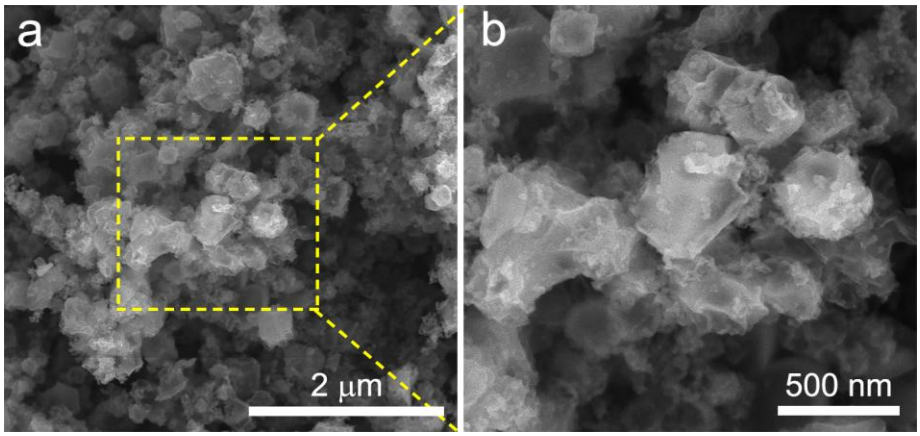

Fig. S9. (a) SEM image and (b) the corresponding enlarged image of NCP.

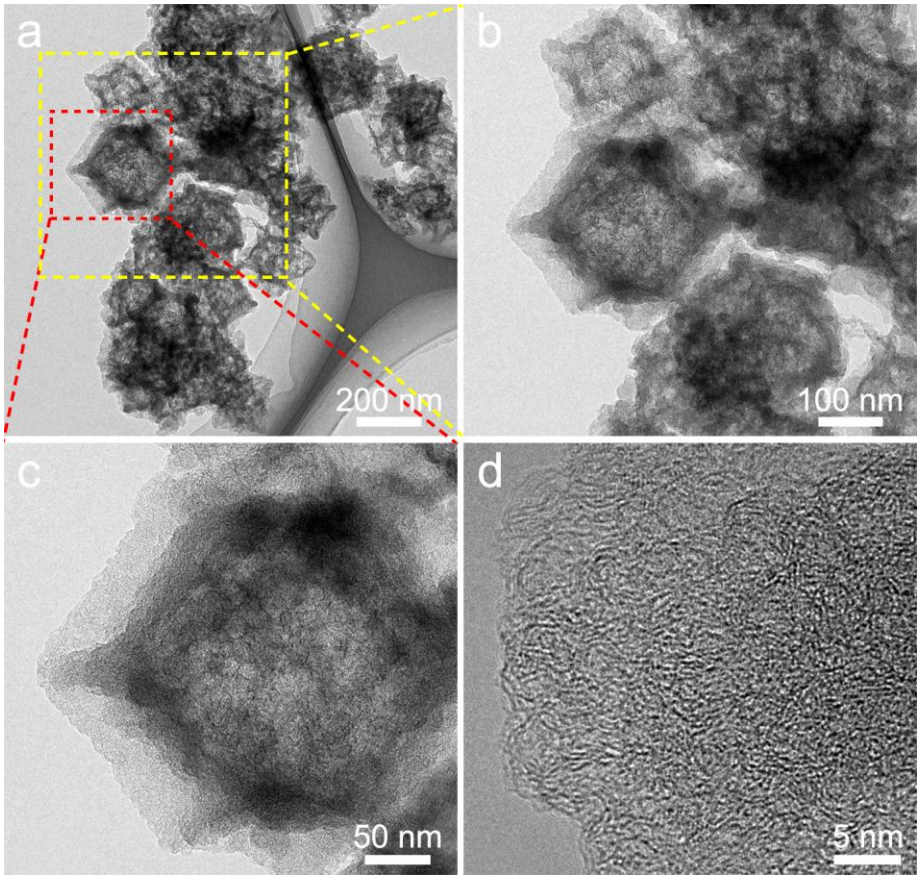

Fig. S10. (a) TEM image and (b,c) the corresponding enlarged images of NCP. (d) HR-TEM image of NCP.

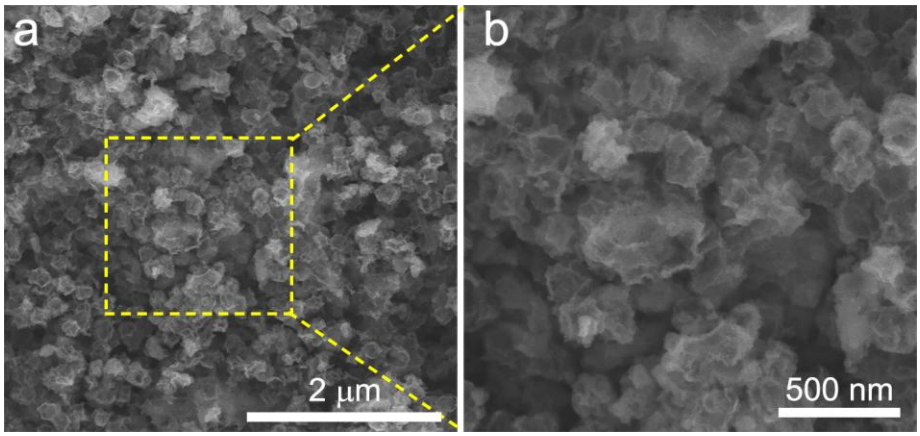

Fig. S11. (a) SEM image and (b) the corresponding enlarged image of NC.

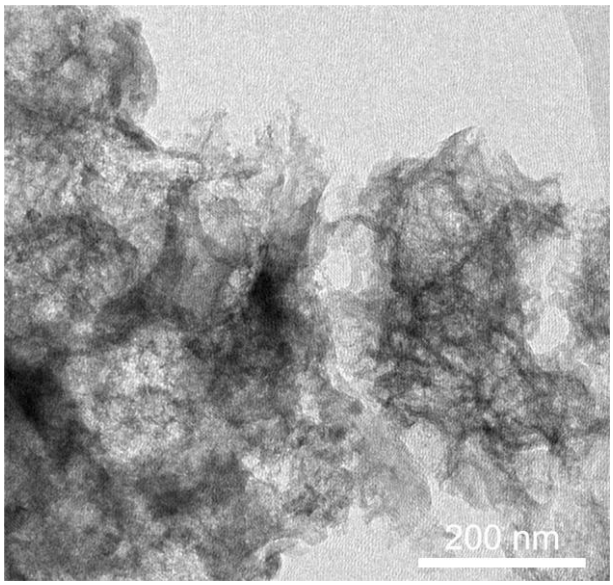

Fig. S12. TEM image of NC.

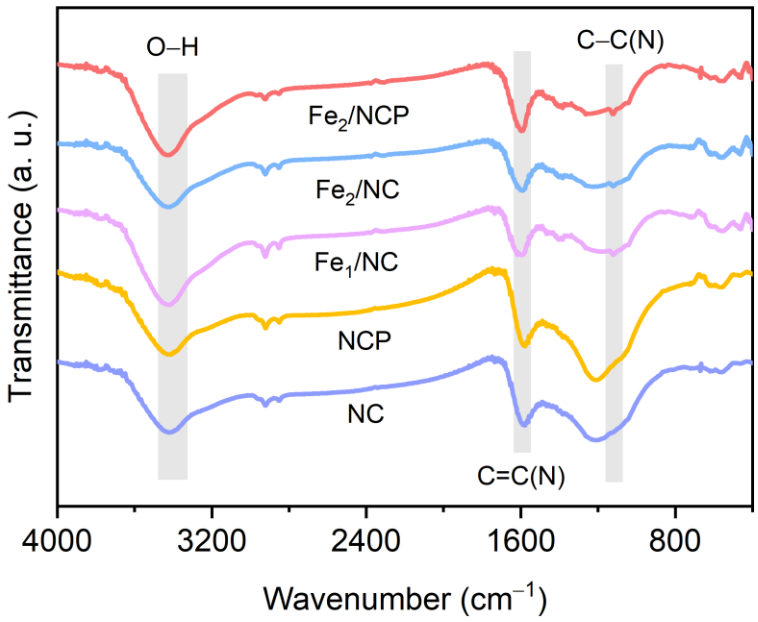

Fig. S13. FT-IR spectra of samples.

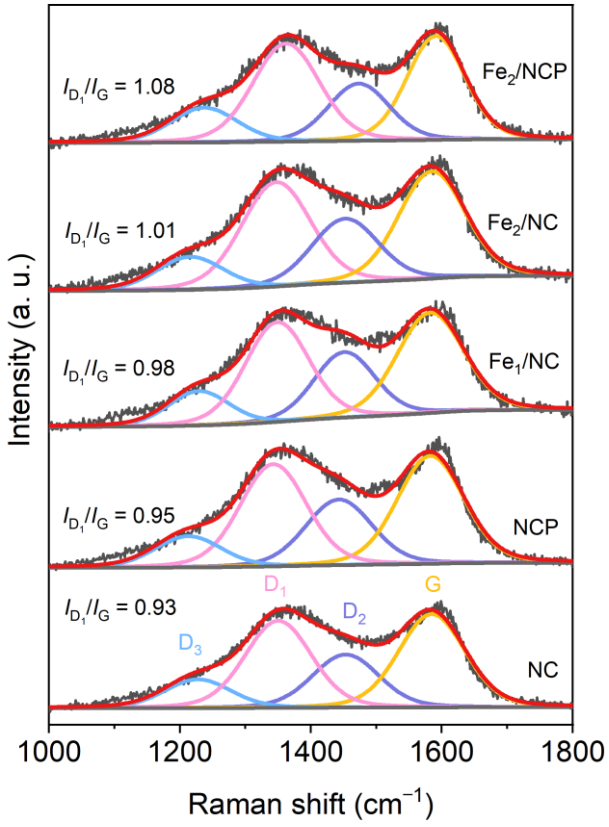

Fig. S14. Raman spectra of samples.

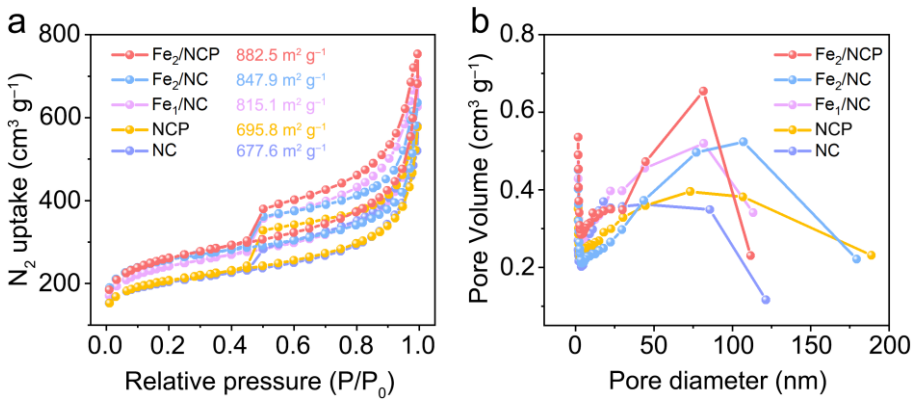

Fig. S15. (a) N_2 adsorption-desorption isotherms and (b) the corresponding pore size distributions of samples.

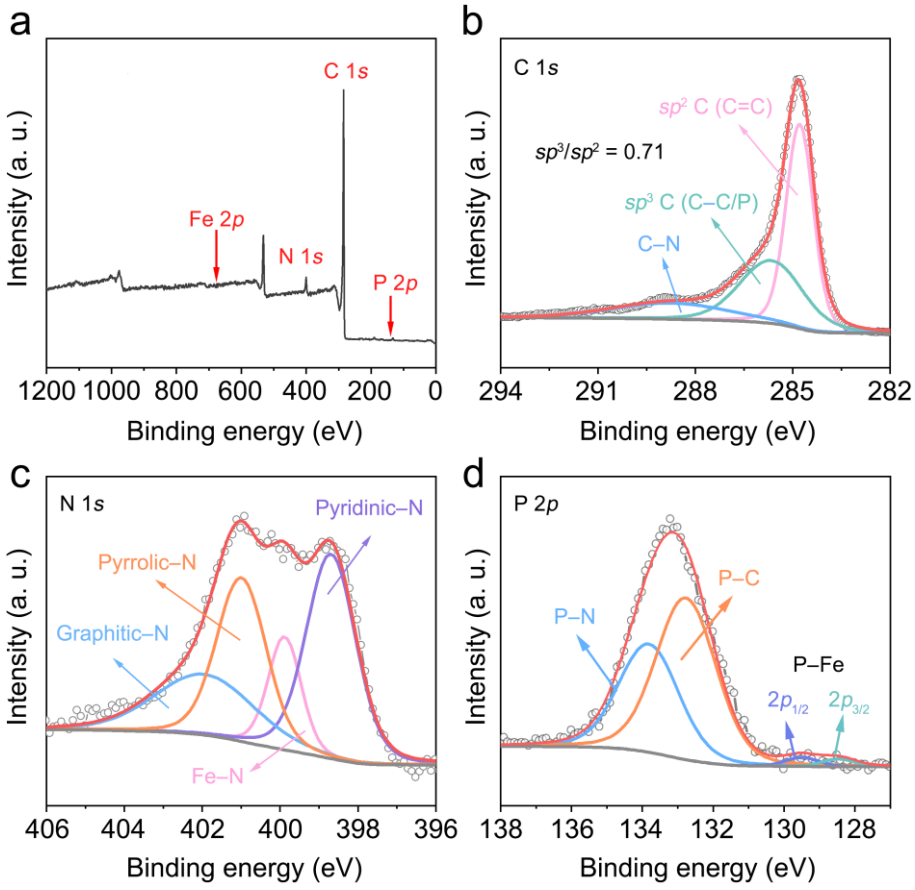

Fig. S16. XPS characterization of Fe_2/NCP. (a) XPS survey scan, (b) C 1*s*, (c) N 1*s* and (d) P 2*p* spectra.

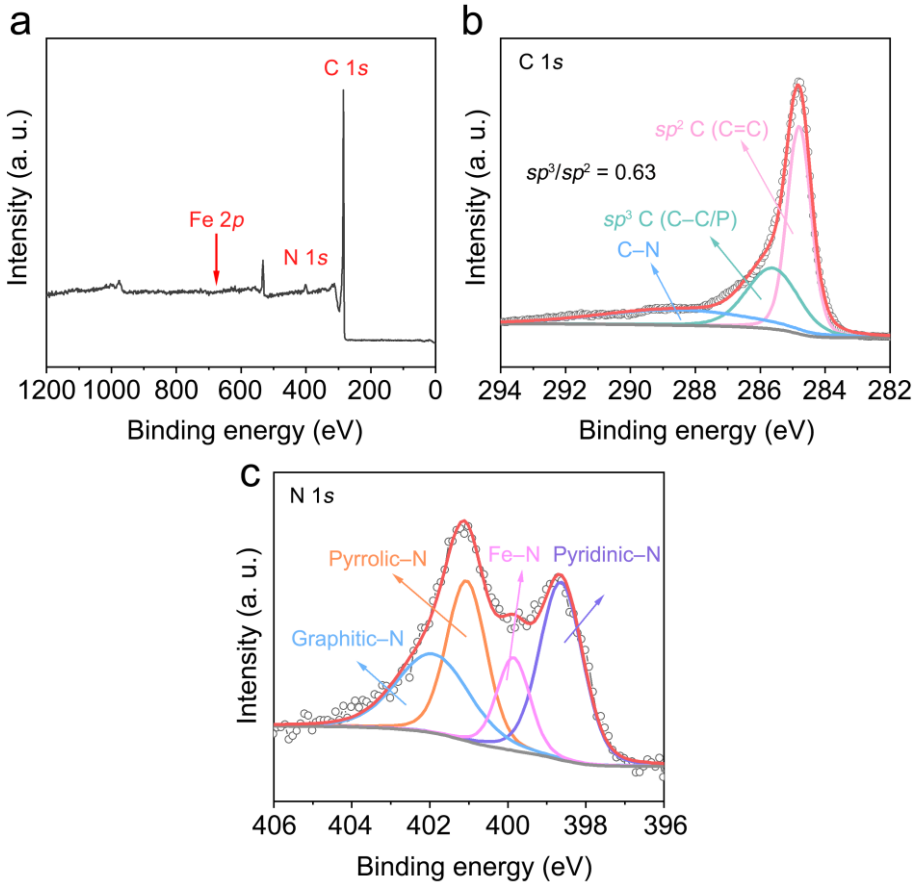

Fig. S17. XPS characterization of Fe_2/NC. (a) XPS survey scan, (b) C 1*s*, and (c) N 1*s* spectra.

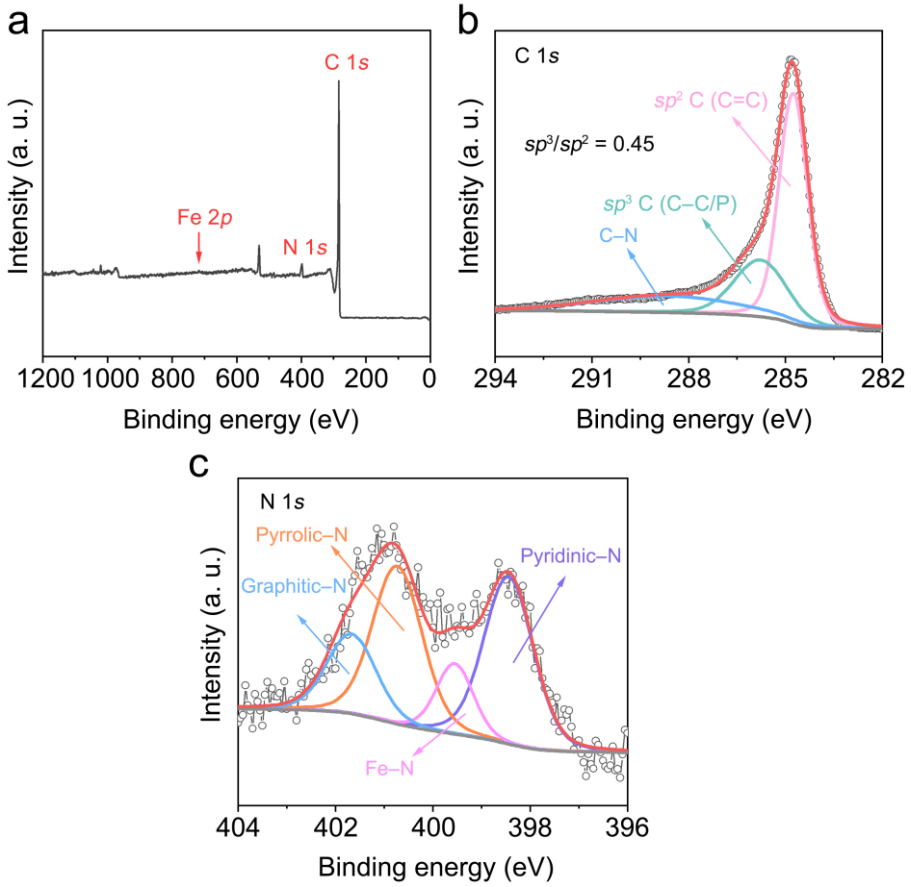

Fig. S18. XPS characterization of Fe_1/NC. (a) XPS survey scan, (b) C 1*s*, and (c) N 1*s* spectra.

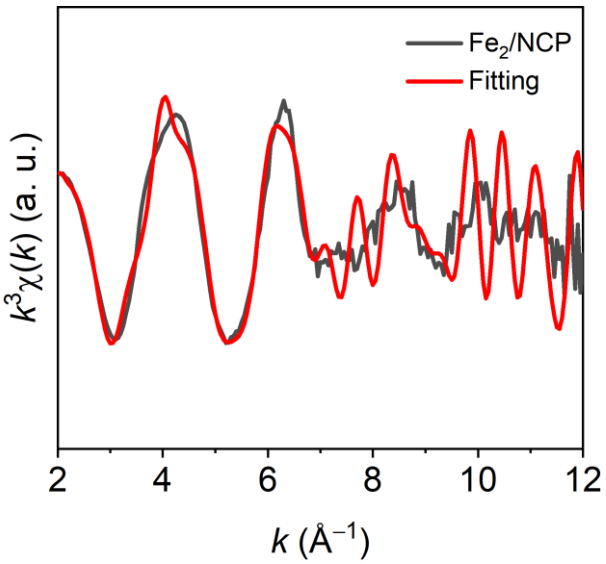

Fig. S19. FT-EXAFS fitting curve of Fe_2/NCP in *k* space.

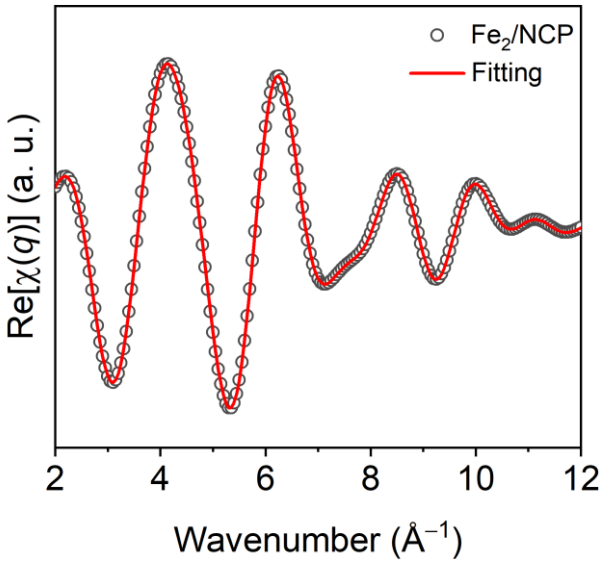

Fig. S20. FT-EXAFS fitting curve of Fe_2/NCP in *q* space.

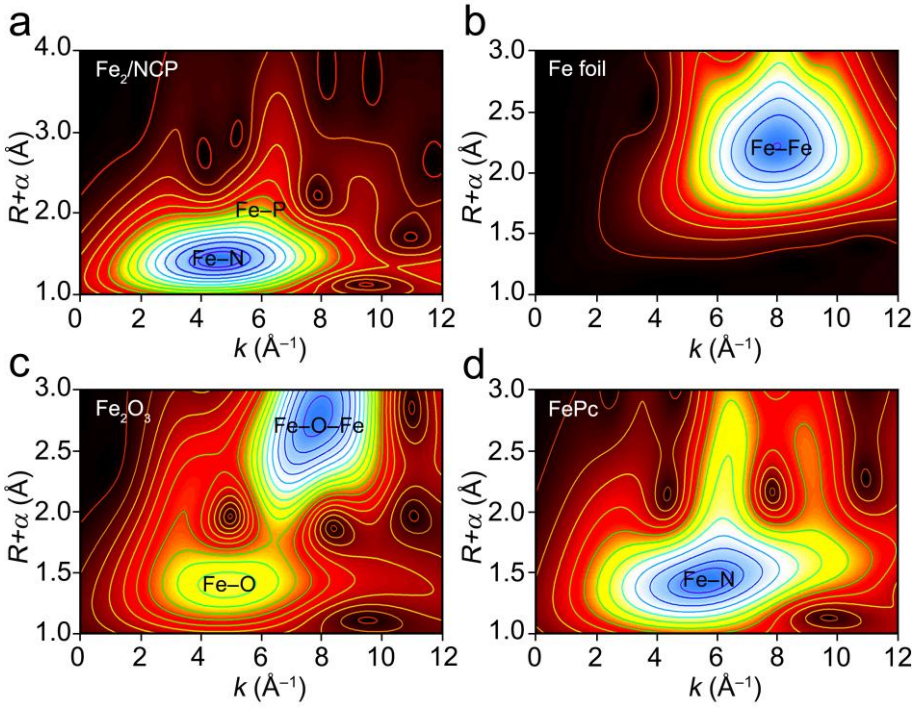

Fig. S21. Wavelet-transform of EXAFS spectra of (a) Fe_2/NCP, (b) Fe foil, (c) Fe_2O_3, and (d) FePc.

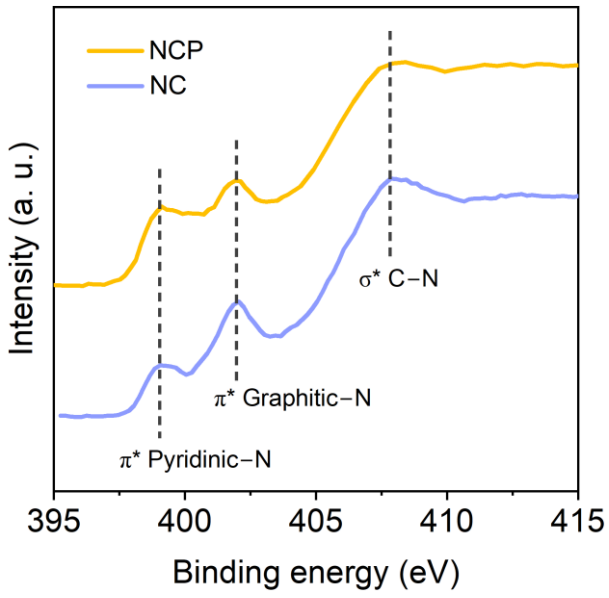

Fig. S22. N K-edge XANES spectra of NCP and NC.

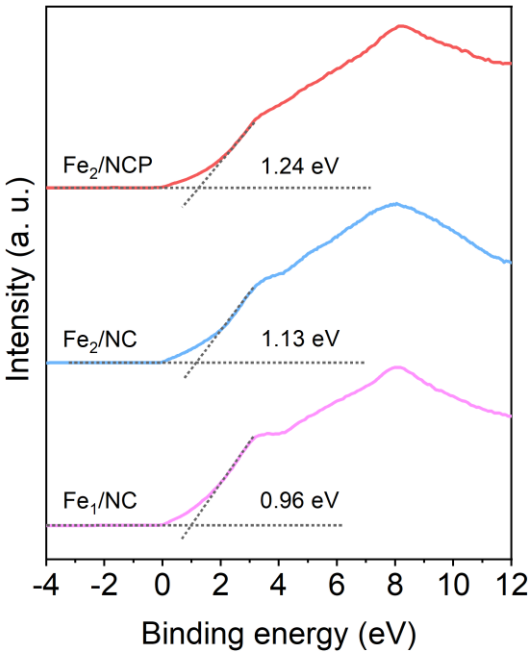

Fig. S23. UPS valence band spectra of Fe_2/NCP, Fe_2/NC, and Fe_1/NC.

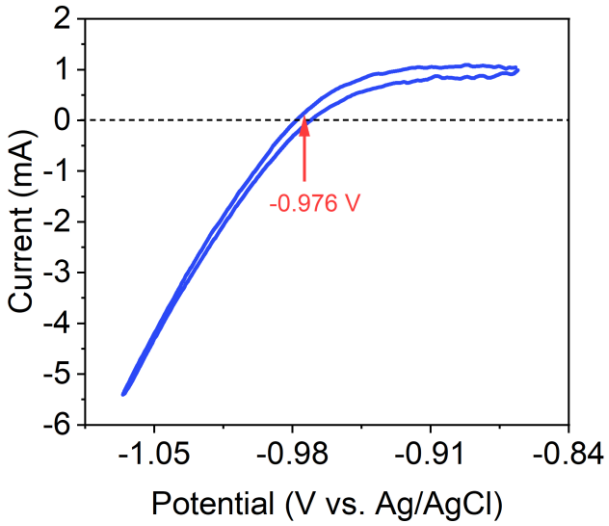

Fig. S24. The calibration curve of reference electrode in 0.1 M KOH. *E* (vs. RHE) = *E* (vs. Ag/AgCl) + 0.976 V.

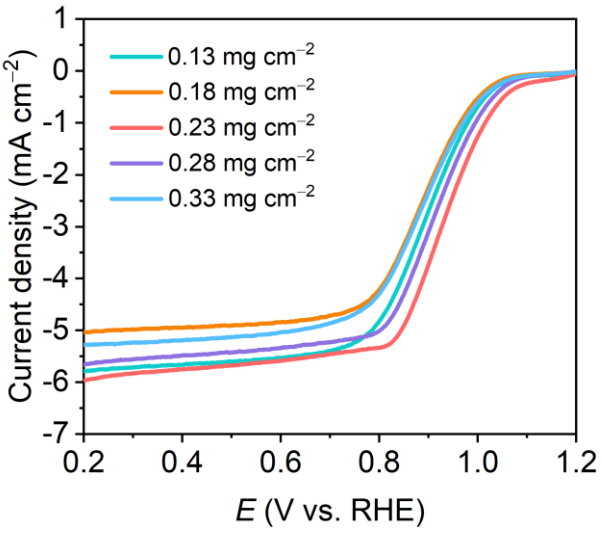

Fig. S25. ORR LSV curves of Fe_2/NCP with different loadings in 0.1 M KOH.

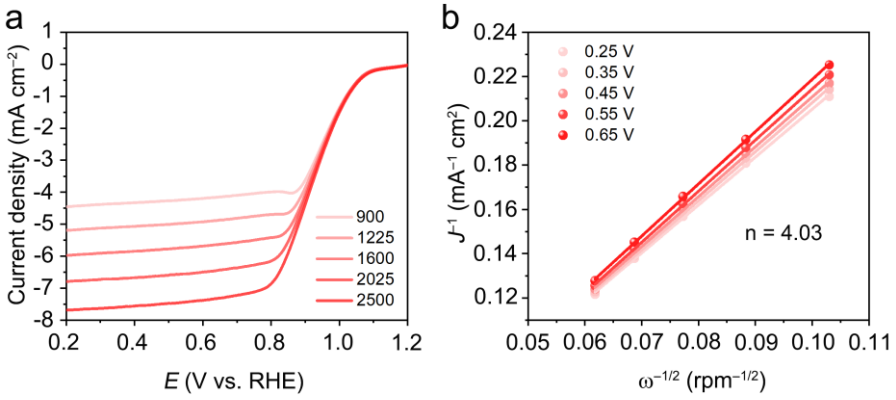

Fig. S26. (a) ORR LSV curves of Fe_2/NCP at different rotating speeds in 0.1 M KOH. (b) The corresponding K-L plots and electron-transfer number.

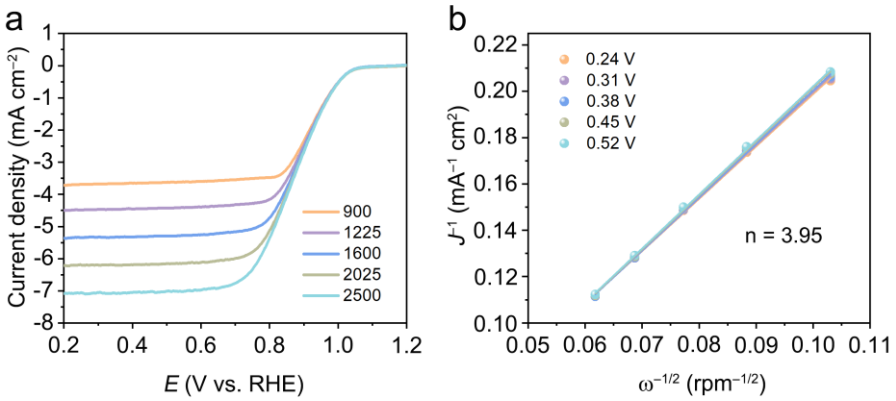

Fig. S27 (a) ORR LSV curves of Fe_2/NC at different rotating speeds in 0.1 M KOH. (b) The corresponding K-L plots and electron-transfer number.

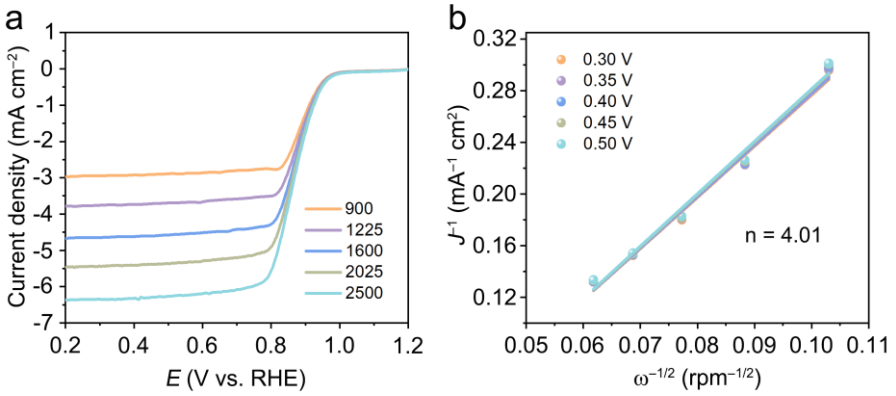

Fig. S28. (a) ORR LSV curves of Fe_1/NC at different rotating speeds in 0.1 M KOH. (b) The corresponding K-L plots and electron-transfer number.

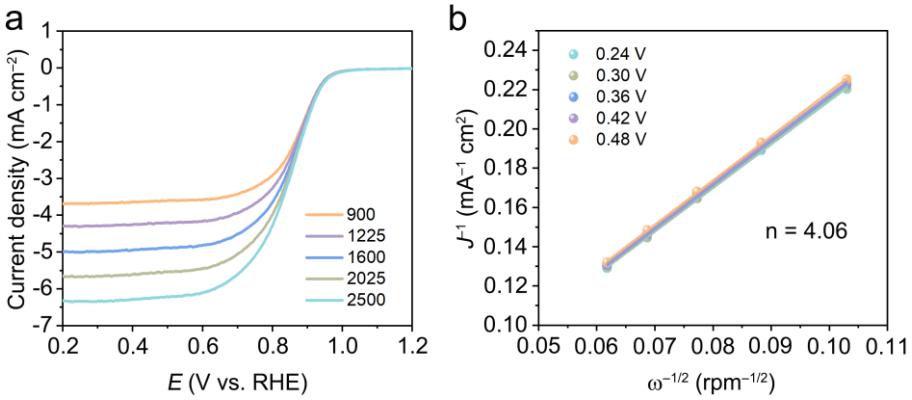

Fig. S29. (a) ORR LSV curves of Pt/C at different rotating speeds in 0.1 M KOH. (b) The corresponding K-L plots and electron-transfer number.

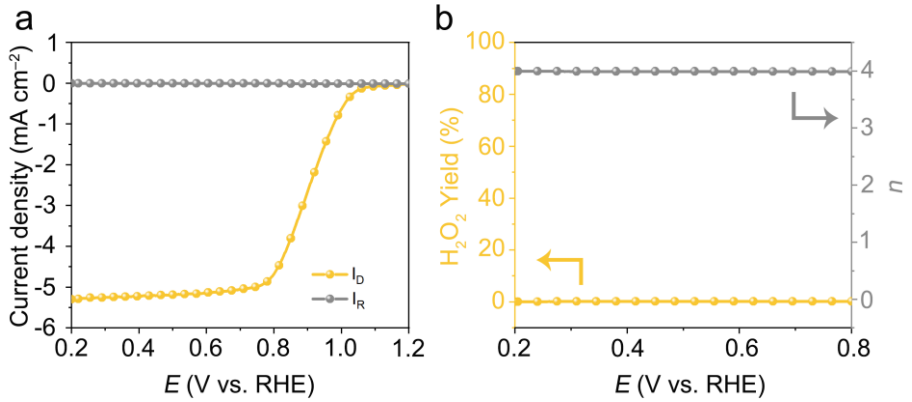

Fig. S30. (a) RRDE measurements and (b) the corresponding electron transfer number and H_2O_2 yield of Fe_2/NC in 0.1 M KOH.

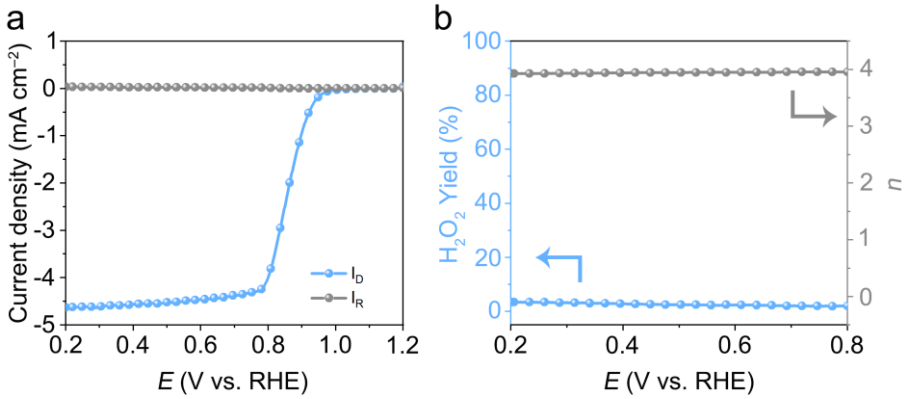

Fig. S31. (a) RRDE measurements and (b) the corresponding electron transfer number and H_2O_2 yield of Fe_1/NC in 0.1 M KOH.

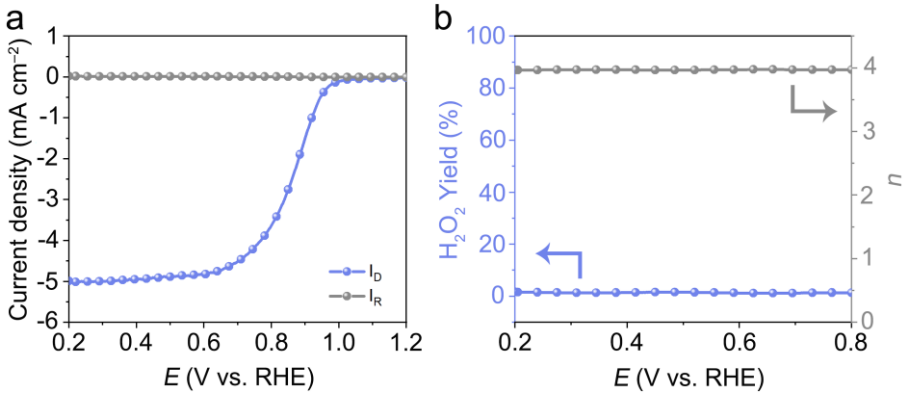

Fig. S32. (a) RRDE measurements and (b) the corresponding electron transfer number and H_2O_2 yield of Pt/C in 0.1 M KOH.

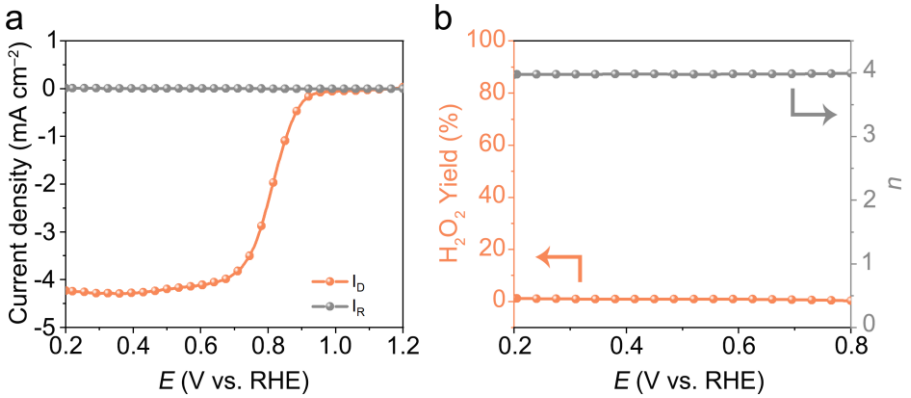

Fig. S33. (a) RRDE measurements and (b) the corresponding electron transfer number and H_2O_2 yield of NCP in 0.1 M KOH.

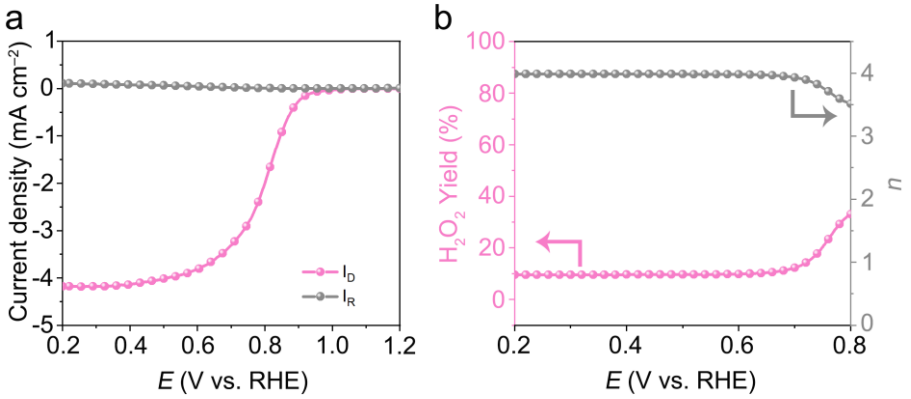

Fig. S34. (a) RRDE measurements and (b) the corresponding electron transfer number and H_2O_2 yield of NC in 0.1 M KOH.

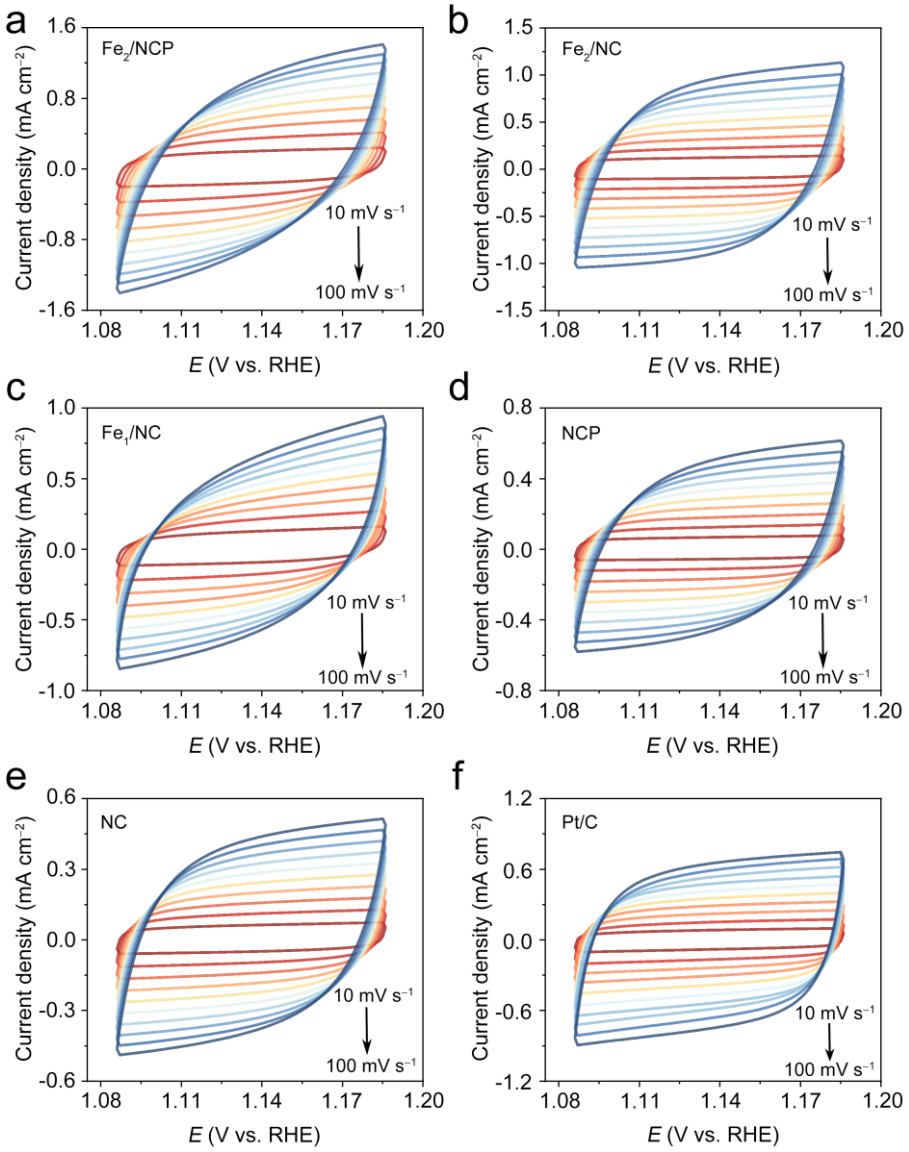

Fig. S35. CV curves of (a) Fe_2/NCP, (b) Fe_2/NC, (c) Fe_1/NC, (d) NCP, (e) NC, and (f) 20 wt% Pt/C in 0.1 M KOH.

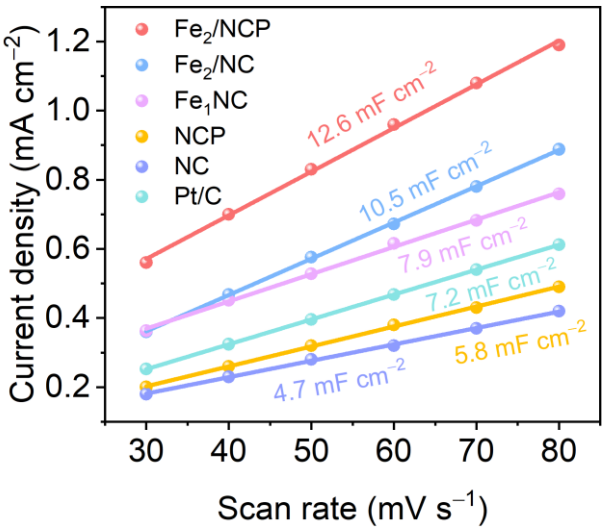

Fig. S36. The calculated C_{dl} values.

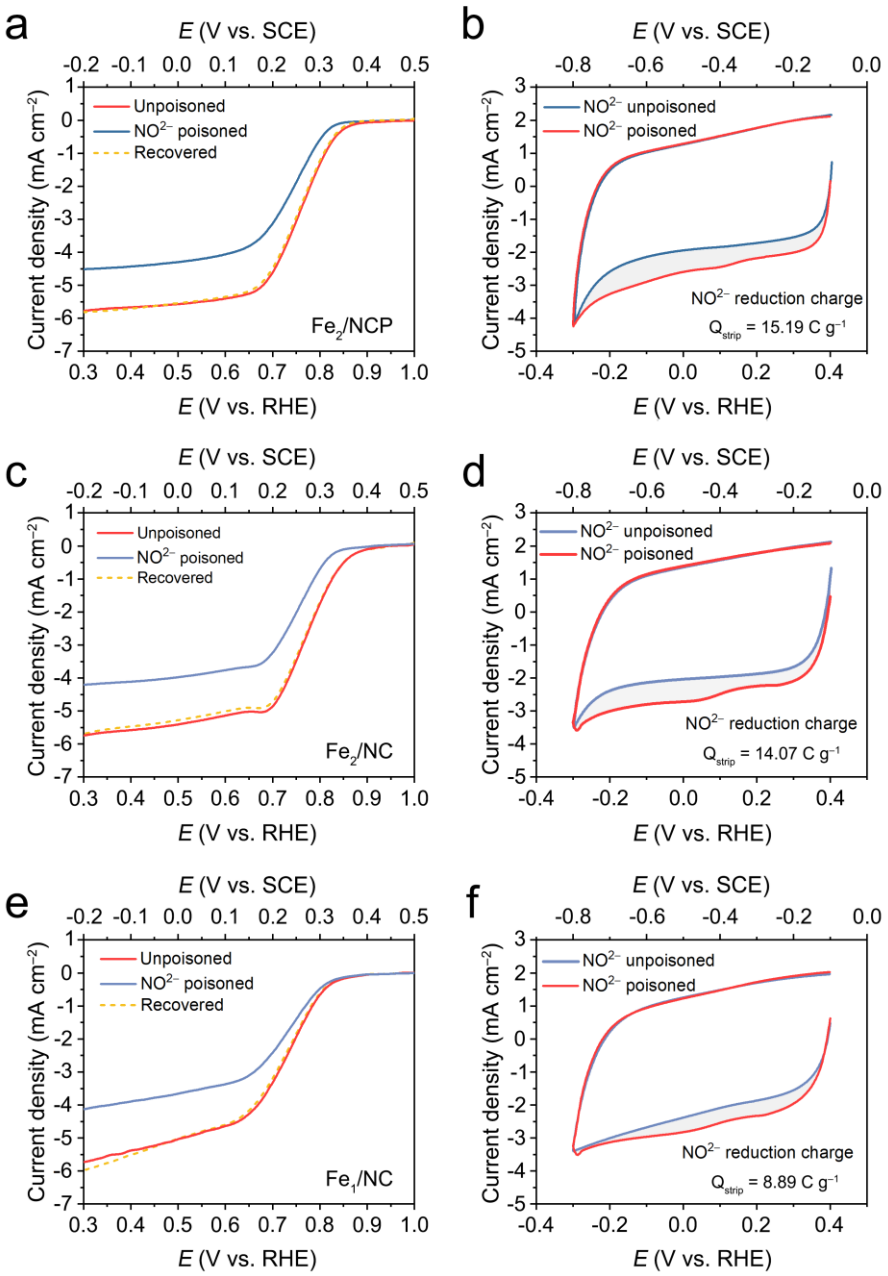

Fig. S37. Determination of site density of Fe_2/NCP, Fe_2/NC, and Fe_1/NC by reversible nitrite poisoning. (a,c,e) LSV curves before, during, and after nitrite adsorption. (b,d,f) CV curves before and during nitrite adsorption in the nitrite reductive stripping region. 0.5 M acetate buffer at pH 5.2. Catalyst loading: 0.27 mg cm^{-2}.

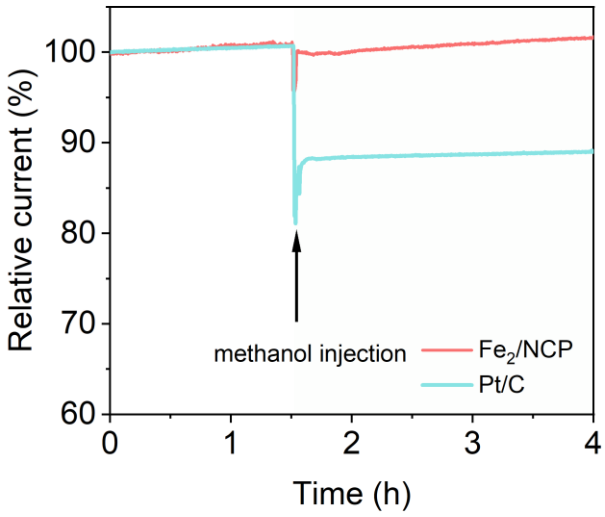

Fig. S38. Methanol tolerance evaluation in 0.1 M KOH.

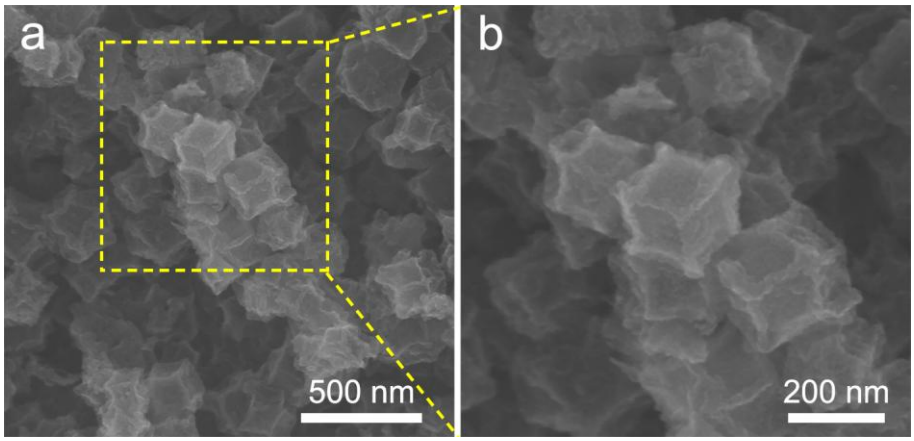

Fig. S39. (a) SEM image and (b) the corresponding enlarged image of Fe_2/NCP after 40000 potential cycles in 0.1 M KOH.

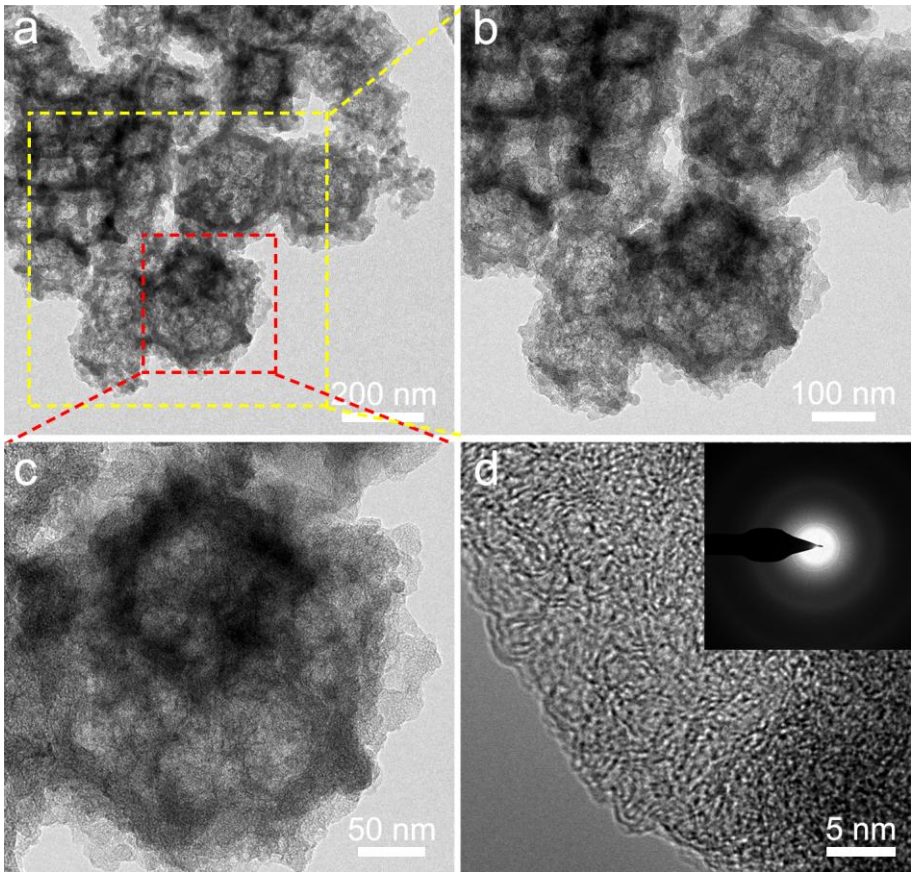

Fig. S40. Morphology characterization of Fe_2/NCP after 40000 potential cycles in 0.1 M KOH. (a) TEM image and (b, c) the corresponding enlarged images. (d) HR-TEM image and SAED pattern.

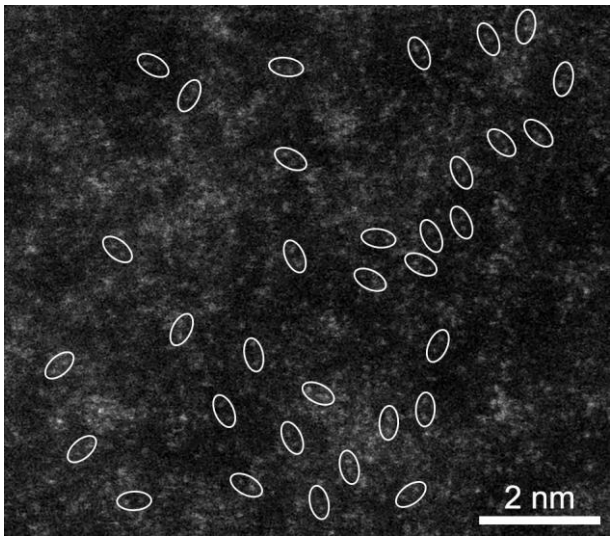

Fig. S41. AC HAADF-STEM image of Fe_2/NCP after 40000 potential cycles in 0.1 M KOH.

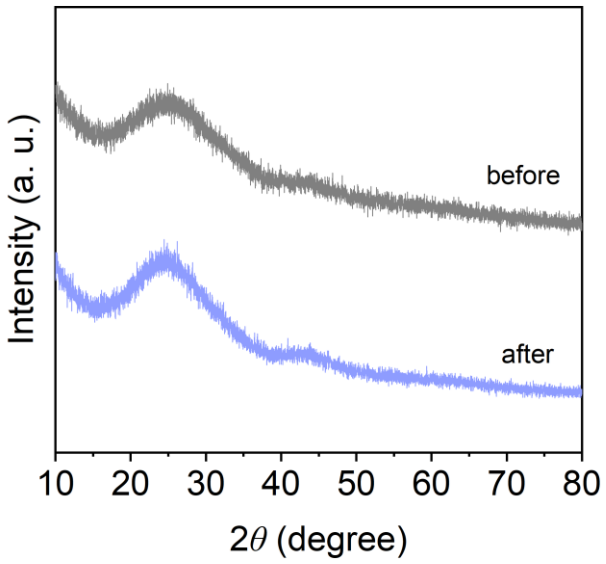

Fig. S42. XRD patterns of Fe_2/NCP before and after 40000 potential cycles in 0.1 M KOH.

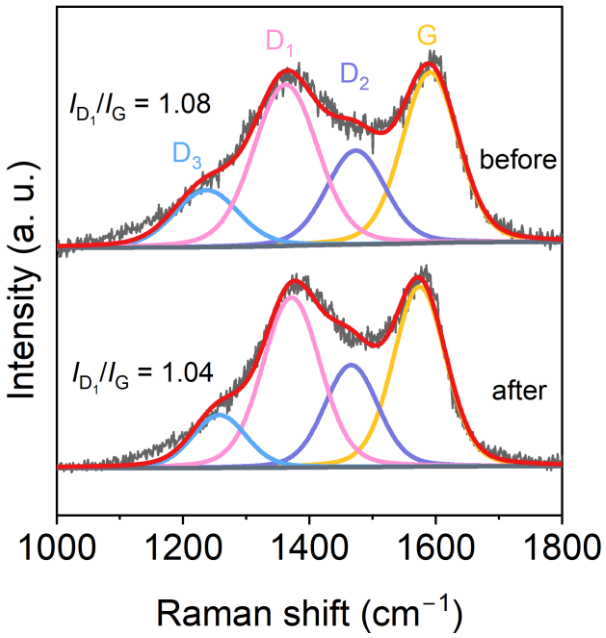

Fig. S43. Raman spectra of Fe_2/NCP before and after 40000 potential cycles in 0.1 M KOH.

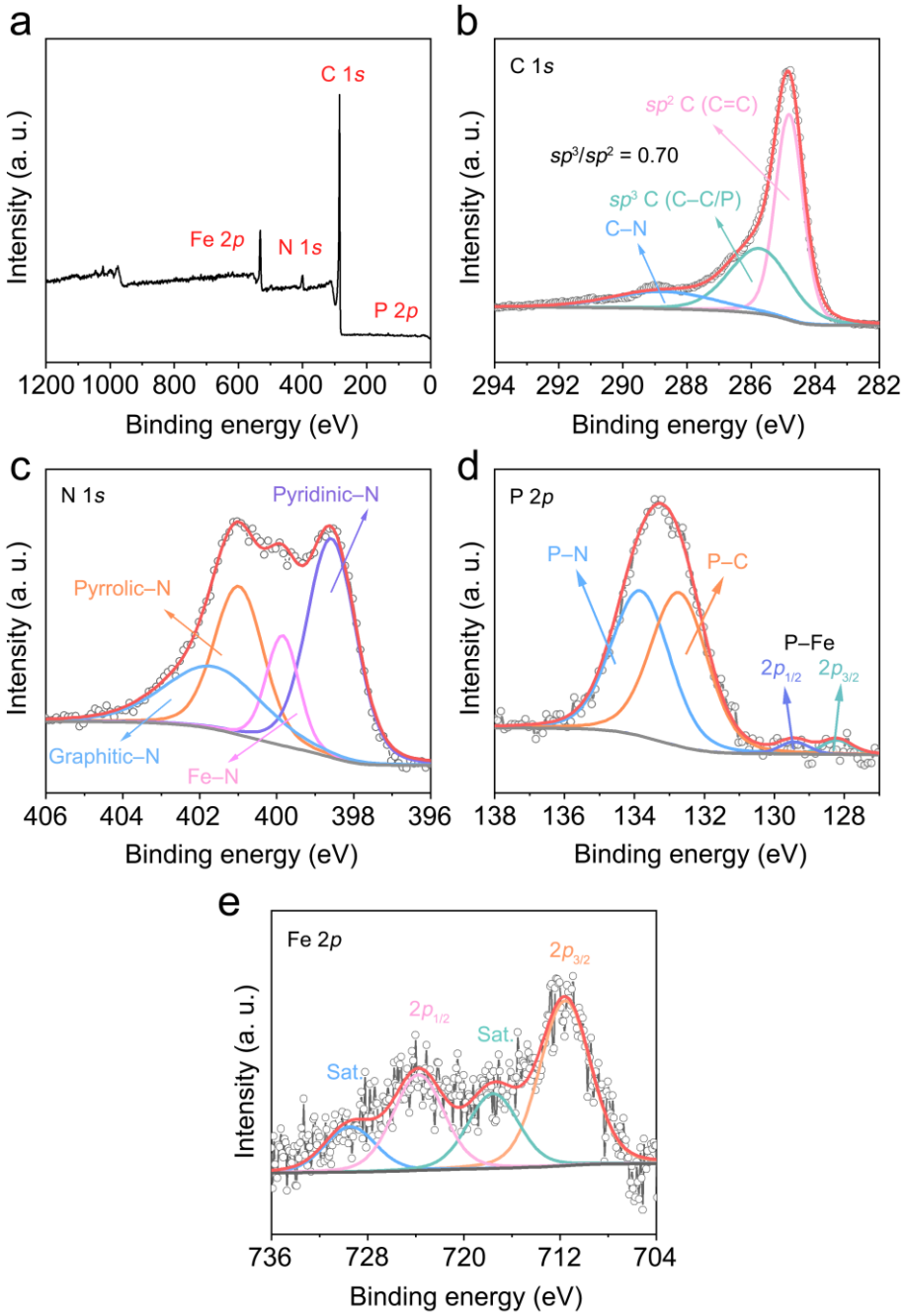

Fig. S44. XPS characterization of Fe_2/NCP after 40000 potential cycles in 0.1 M KOH. (a) XPS survey scan, (b) C 1*s*, (c) N 1*s*, (d) P 2*p*, and (e) Fe 2*p* spectra.

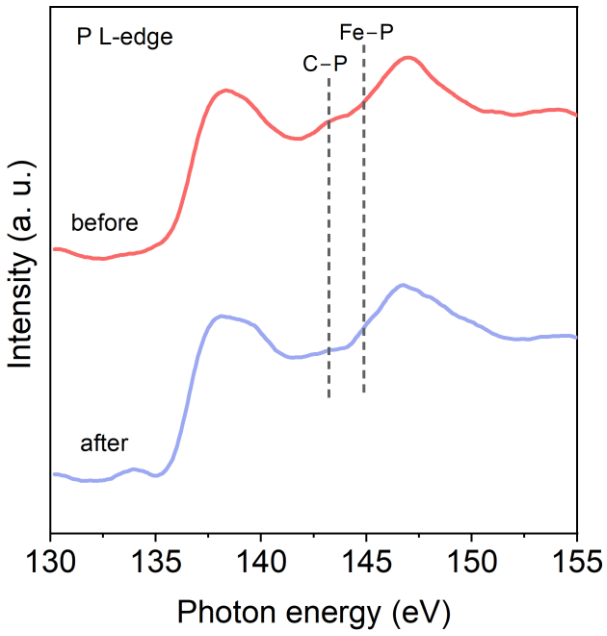

Fig. S45. P L-edge XANES spectra of Fe_2/NCP before and after 40000 potential cycles in 0.1 M KOH.

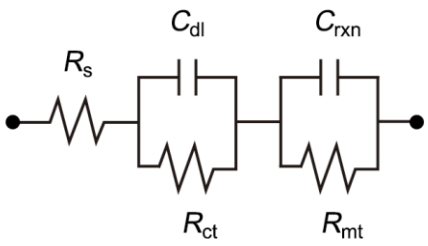

Fig. S46. The equivalent circuit fitting model. The fitting elements were assigned to the solution resistance (R_s), double-layer capacitance of catalyst layer (C_{dl}), the charge transfer resistance (R_{ct}), mass-transfer resistance (R_{mt}) and capacitance of reaction process (C_{rxn}).

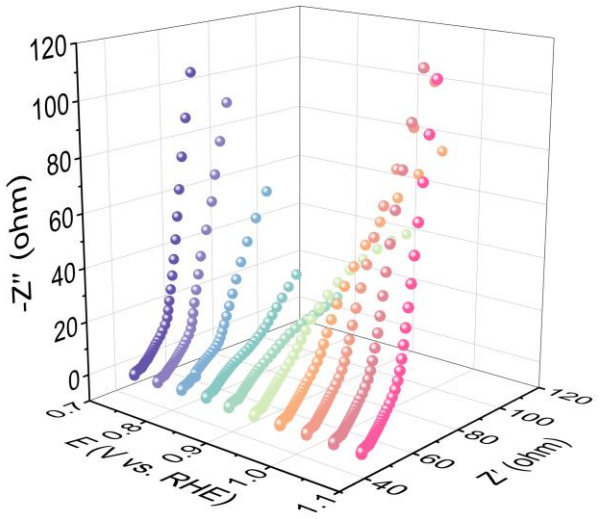

Fig. S47. In situ EIS results of Fe_2/NC in 0.1 M KOH.

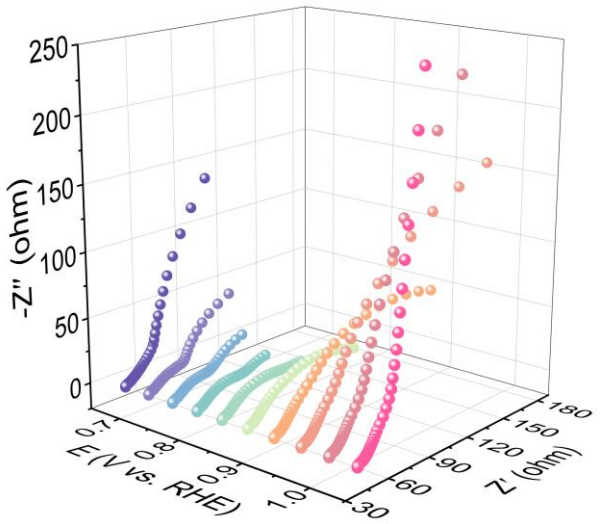

Fig. S48. In situ EIS results of Fe_1/NC in 0.1 M KOH.

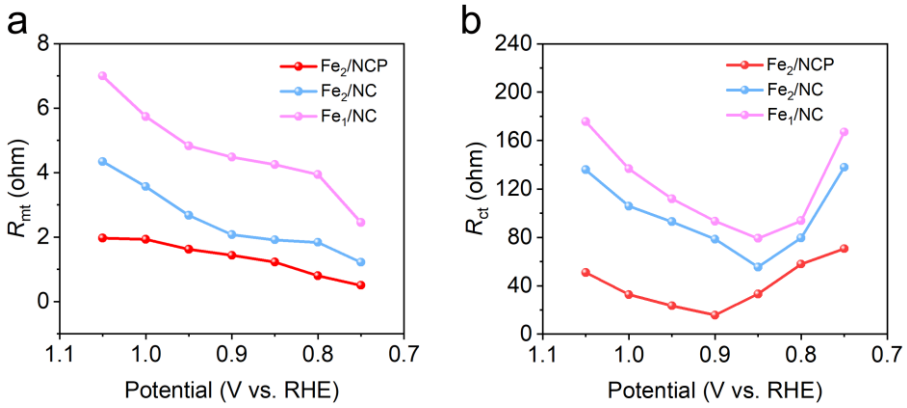

Fig. S49. Comparation of (a) R_{mt} and (b) R_{ct} at different potentials of Fe_2/NCP, Fe_2/NC, and Fe_1/NC in 0.1 M KOH.

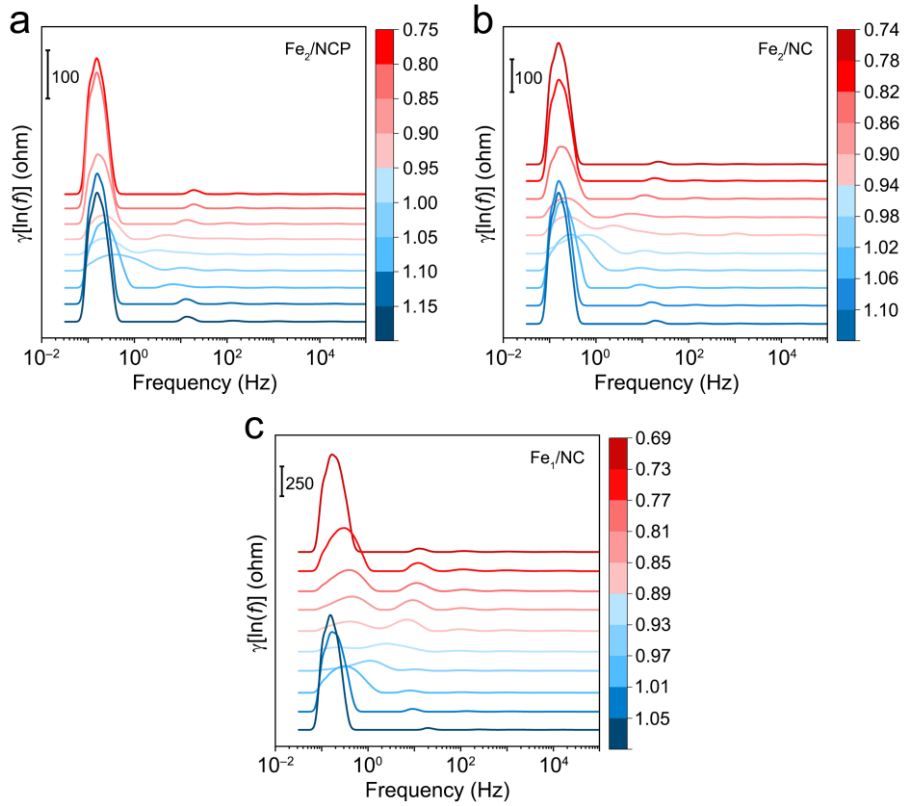

Fig. S50. DRT plots of (a) Fe_2/NCP, (b) Fe_2/NC, and (c) Fe_1/NC obtained by deconvolving the in situ EIS measurement in 0.1 M KOH.

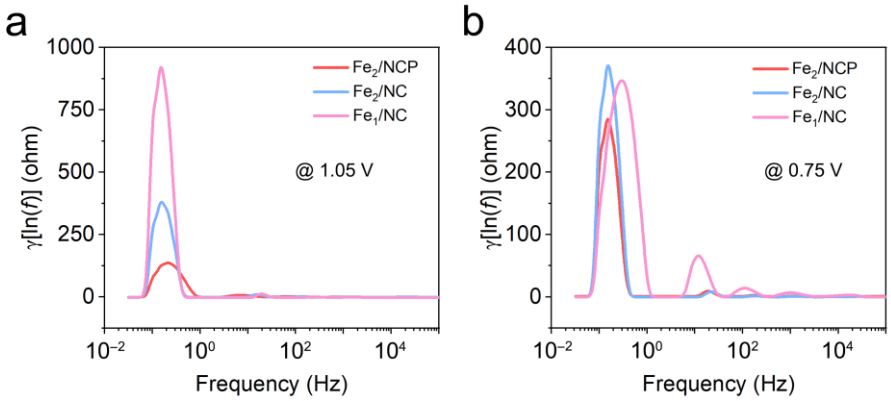

Fig. S51. The DRT analysis of Fe_2/NCP, Fe_2/NC, and Fe_1/NC at (a) 1.05 V and (b) 0.75 V in 0.1 M KOH.

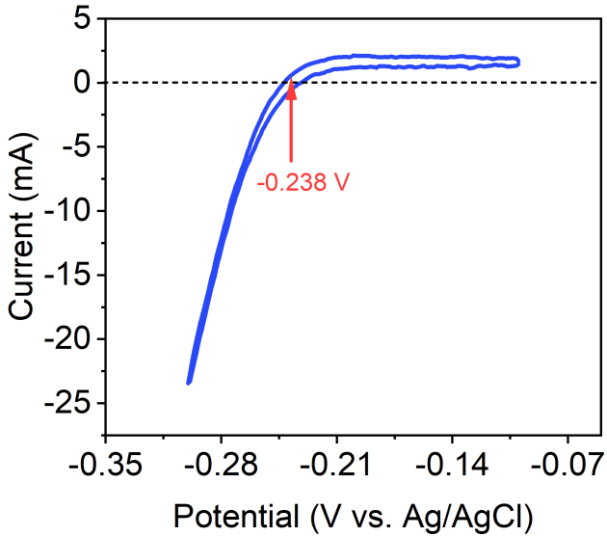

Fig. S52. The calibration curve of reference electrode in 0.5 M H_2SO_4. *E* (vs. RHE) = *E* (vs. Ag/AgCl) + 0.238 V.

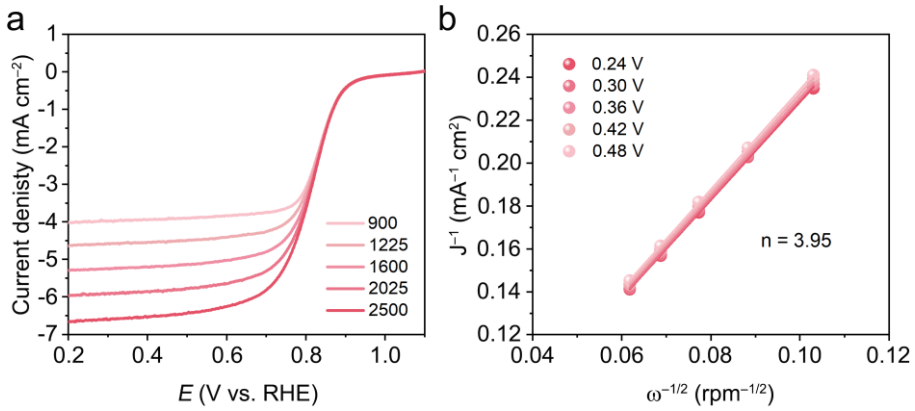

Fig. S53. (a) ORR LSV curves of Fe_2/NCP at different rotating speeds in 0.5 M H_2SO_4. (b) The corresponding K-L plots and electron-transfer number.

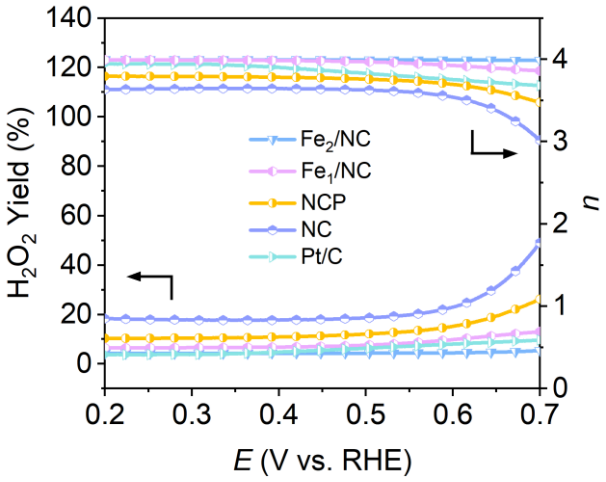

Fig. S54. Electron transfer number and H_2O_2 yield of Fe_2/NC, Fe_1/NC, Pt/C, NCP, and NC in 0.5 M H_2SO_4.

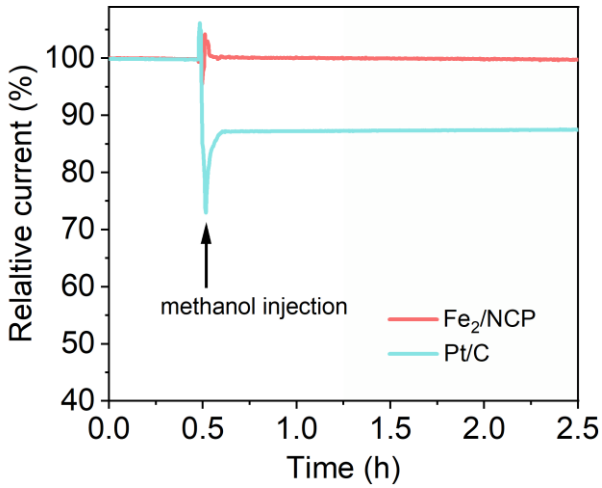

Fig. S55. Methanol tolerance evaluation in 0.5 M H_2SO_4.

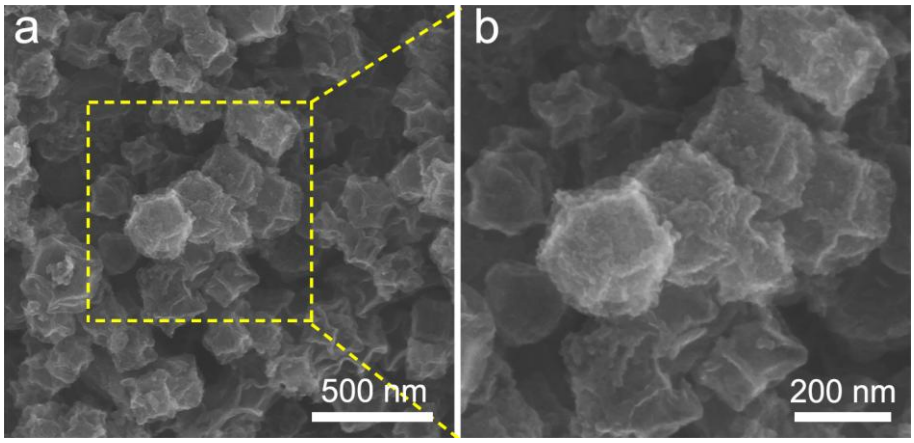

Fig. S56. (a) SEM image and (b) the enlarged image of Fe_2/NCP after 40000 potential cycles in 0.5 M H_2SO_4.

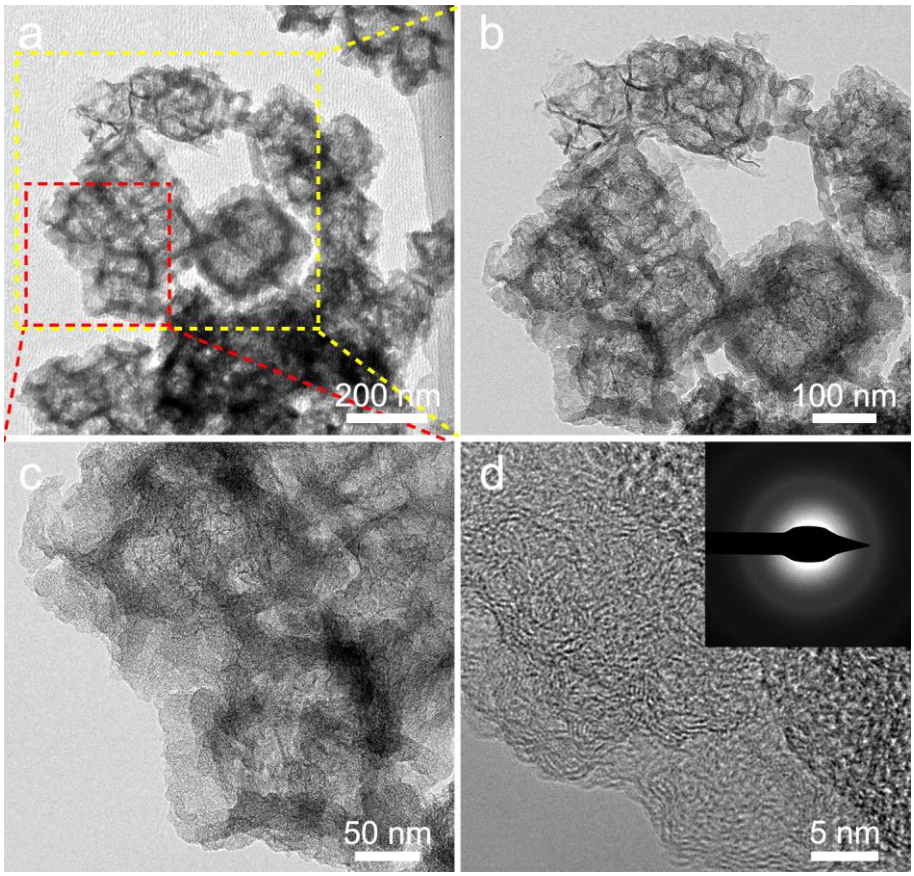

Fig. S57. Morphology characterization of Fe_2/NCP after 40000 potential cycles in 0.5 M H_2SO_4. (a) TEM image and (b, c) the corresponding enlarged images. (d) HR-TEM image and SAED pattern.

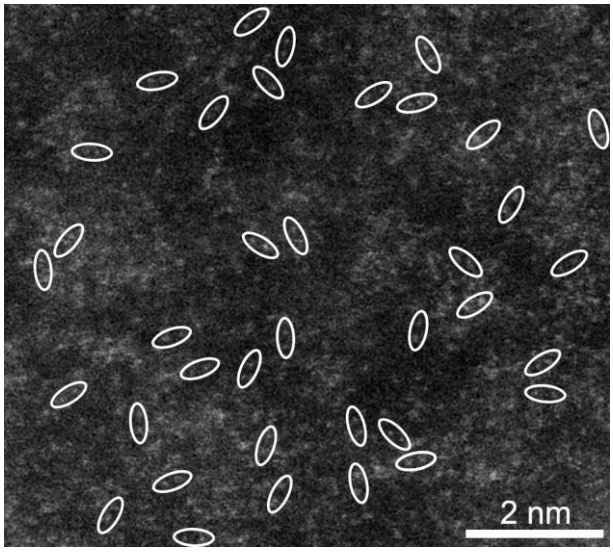

Fig. S58. AC HAADF-STEM image of Fe_2/NCP after 40000 potential cycles in 0.5 M H_2SO_4.

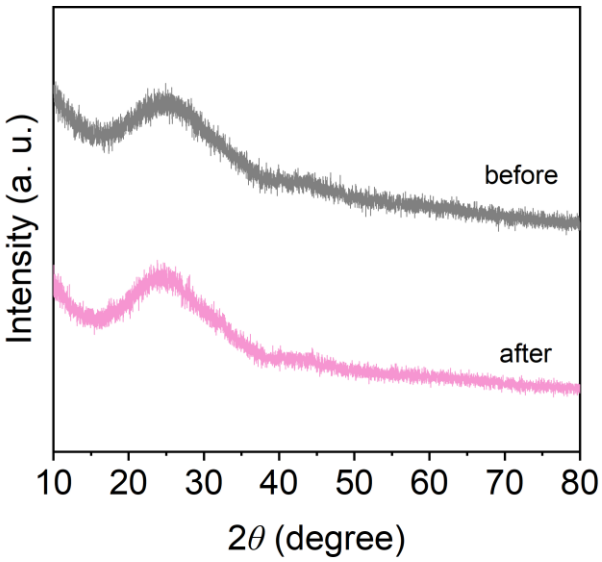

Fig. S59. XRD patterns of Fe_2/NCP before and after 40000 potential cycles in 0.5 M H_2SO_4.

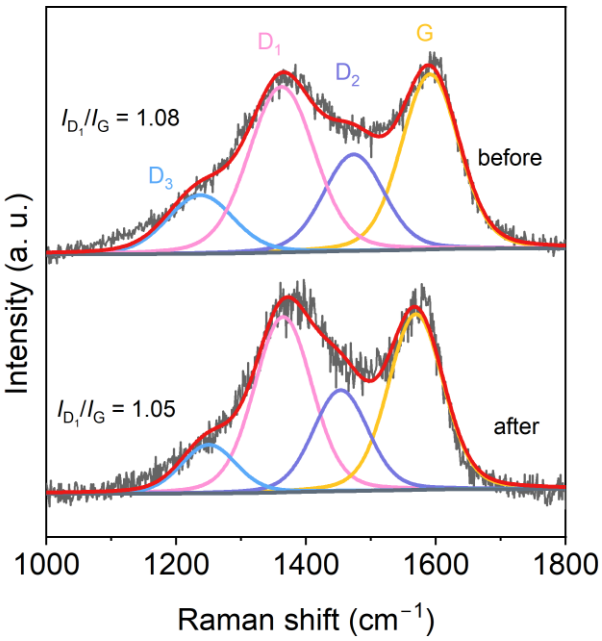

Fig. S60. Raman spectra of Fe_2/NCP before and after 40000 potential cycles in 0.5 M H_2SO_4.

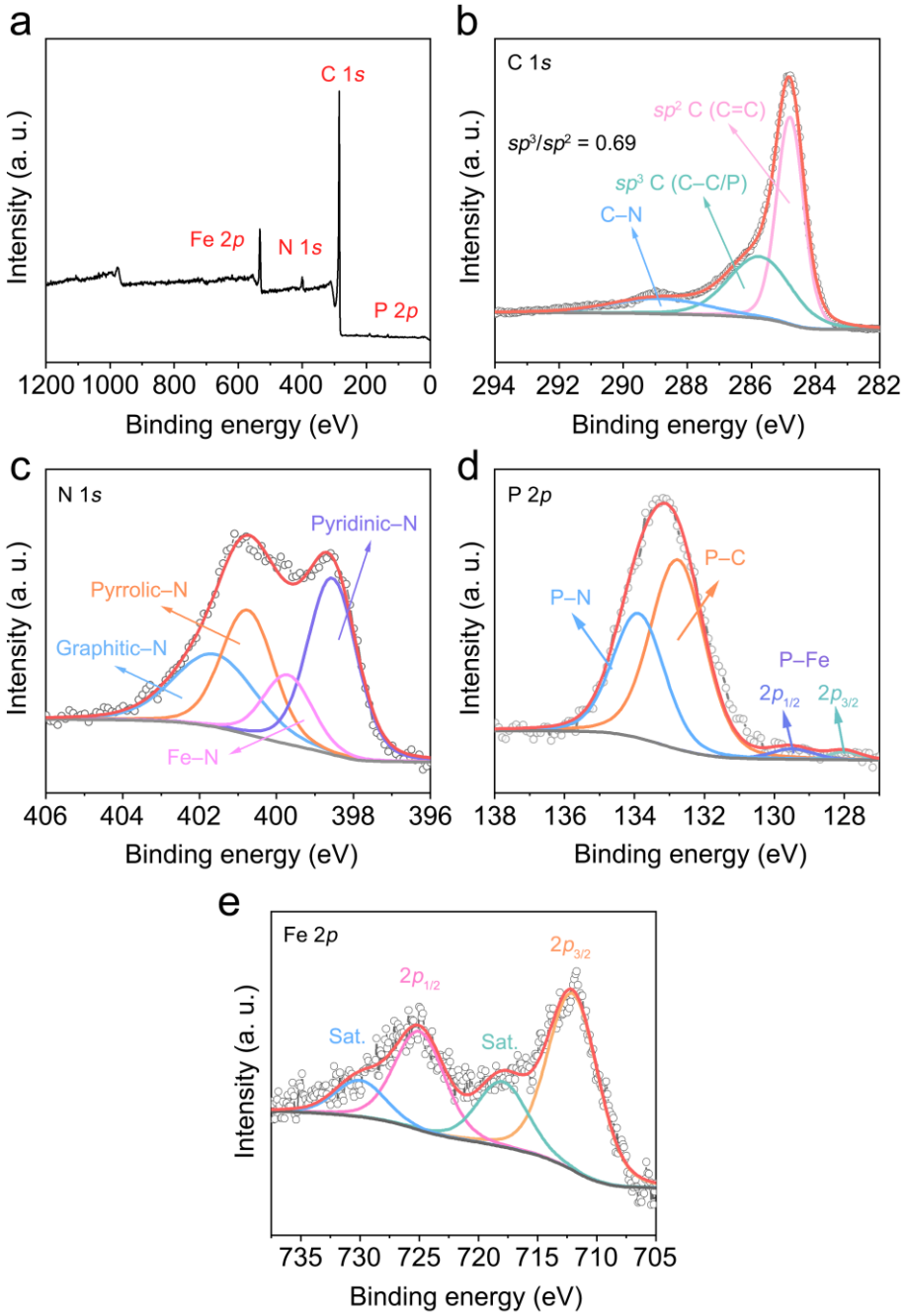

Fig. S61. XPS characterization of Fe_2/NCP after 40000 potential cycles in 0.5 M H_2SO_4. (a) XPS survey scan, (b) C 1*s*, (c) N 1*s*, (d) P 2*p*, and (e) Fe 2*p* spectra.

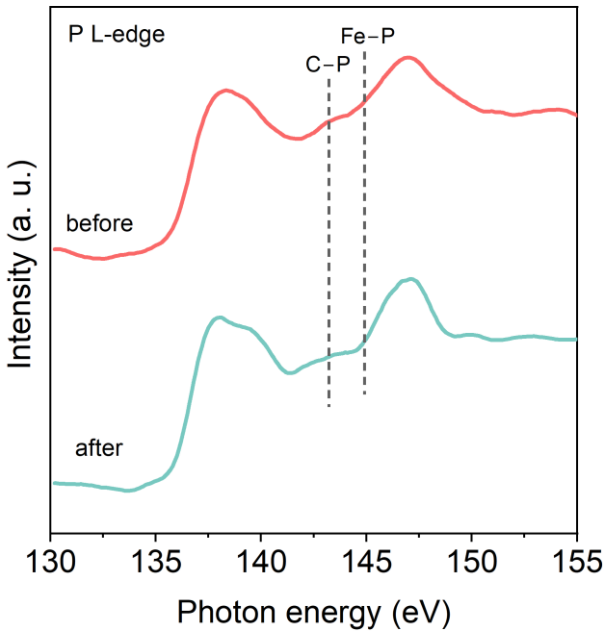

Fig. S62. P L-edge XANES spectra of Fe_2/NCP before and after 40000 potential cycles in 0.5 M H_2SO_4.

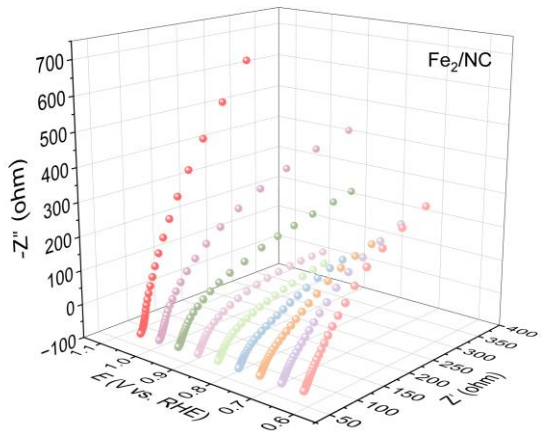

Fig. S63. In situ EIS results of Fe_2/NC in 0.5 M H_2SO_4.

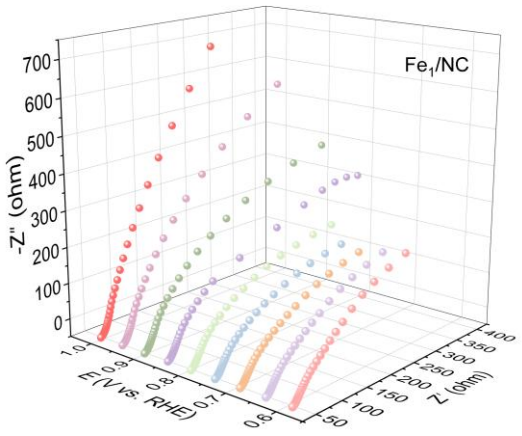

Fig. S64. In situ EIS results of Fe_1/NC in 0.5 M H_2SO_4.

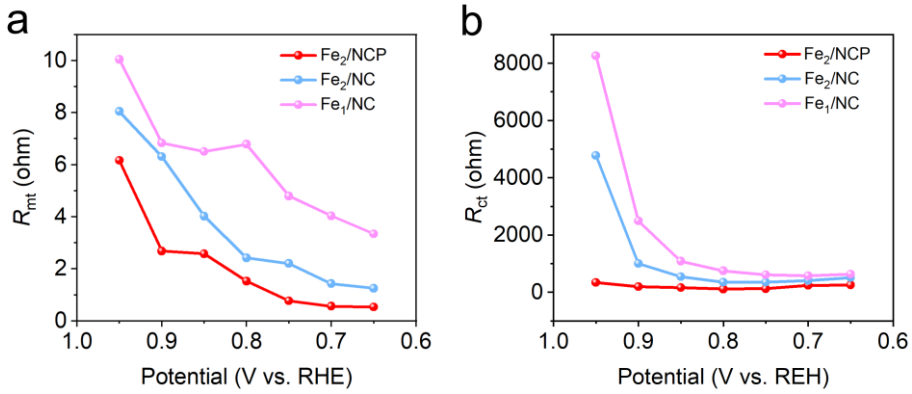

Fig. S65. Comparation of (a) R_{mt} and (b) R_{ct} at different potentials of Fe_2/NCP, Fe_2/NC, and Fe_1/NC in 0.5 M H_2SO_4.

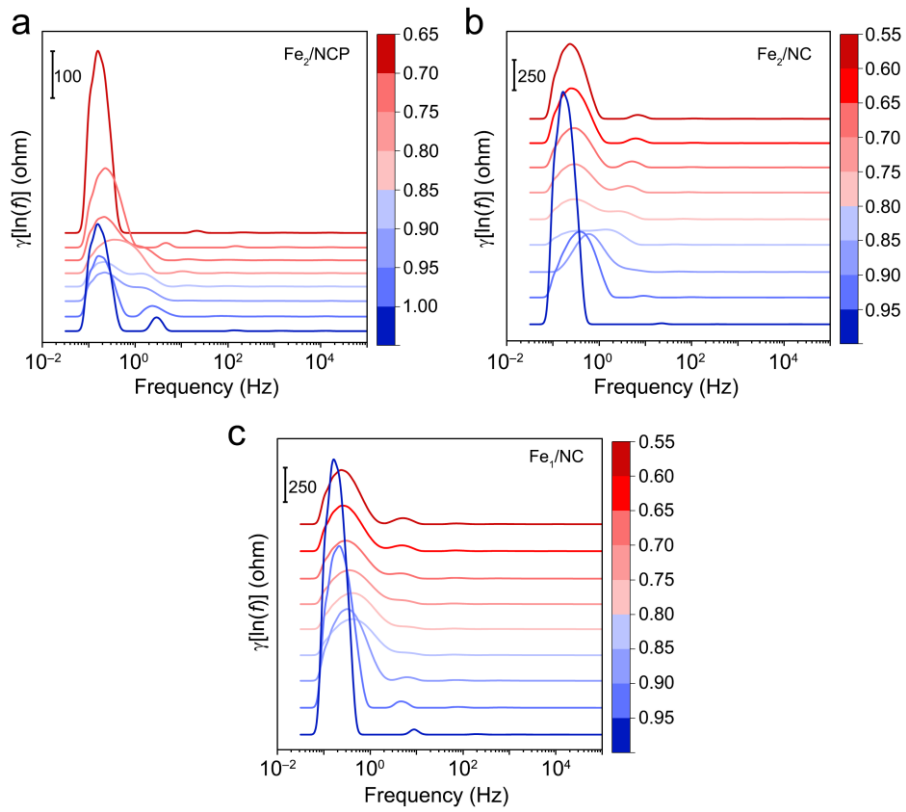

Fig. S66. DRT plots of (a) Fe_2/NCP, (b) Fe_2/NC, and (c) Fe_1/NC obtained by deconvolving the in situ EIS measurement in 0.5 M H_2SO_4.

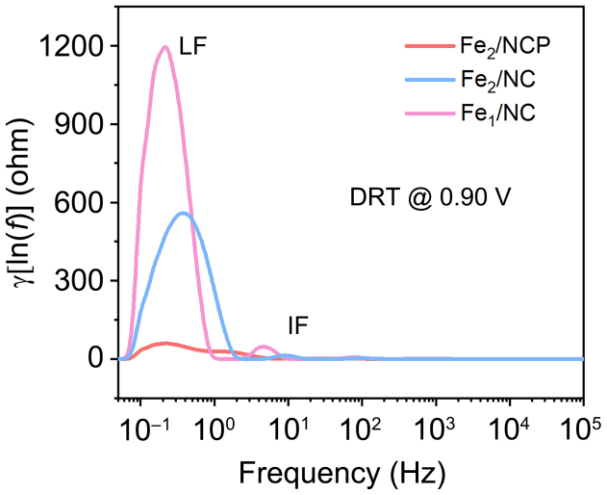

Fig. S67. The DRT analysis of Fe_2/NCP, Fe_2/NC, and Fe_1/NC at 0.90 V in 0.5 M H_2SO_4.

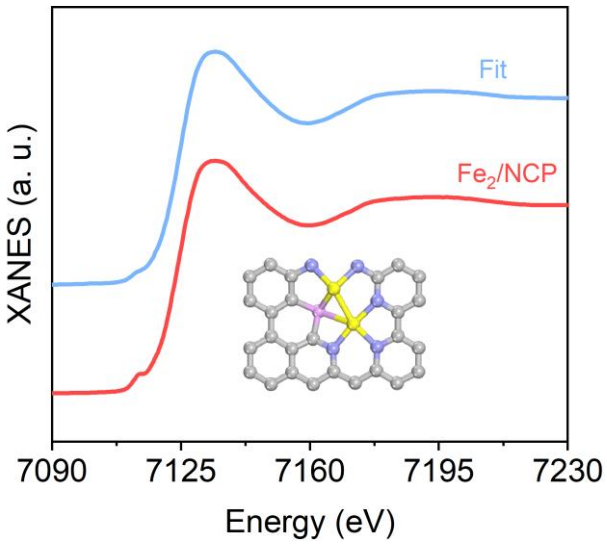

Fig. S68. Experimental Fe K-edge XANES spectrum of Fe_2/NCP and the corresponding theoretical spectrum. Inset: the structure used to simulate the XANES spectra.

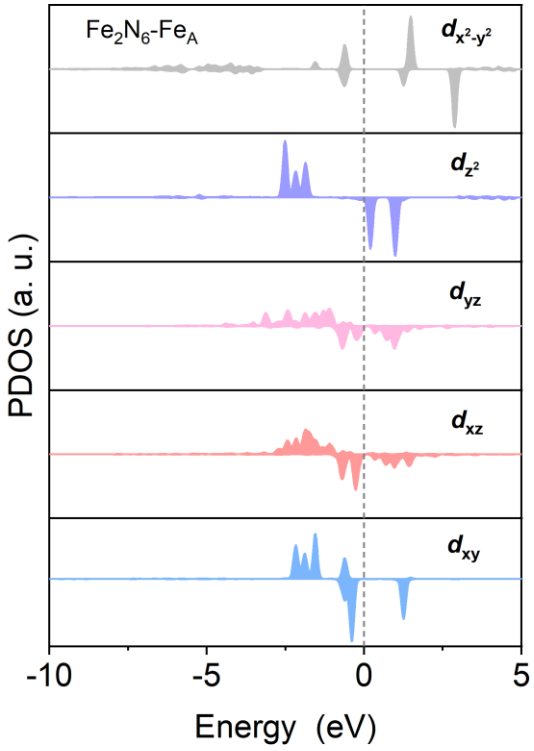

Fig. S69. Orbital-resolved PDOS analysis of Fe_2N_6-Fe_A.

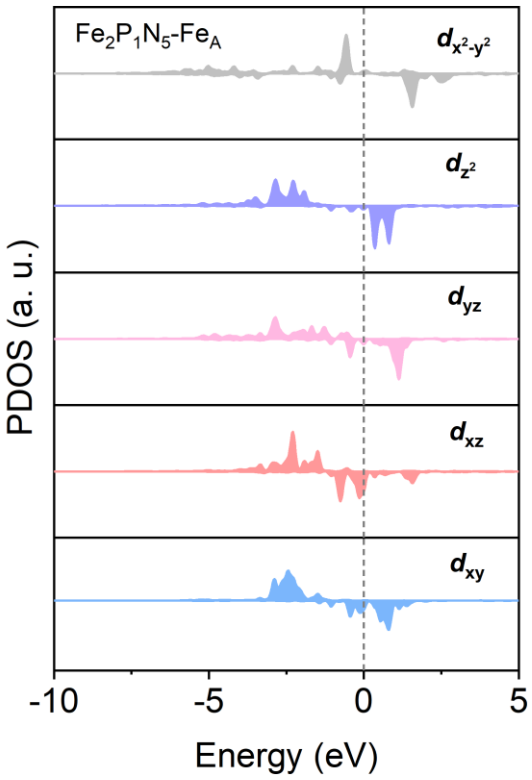

Fig. S70. Orbital-resolved PDOS analysis of $Fe_2P_1N_5$-Fe_A.

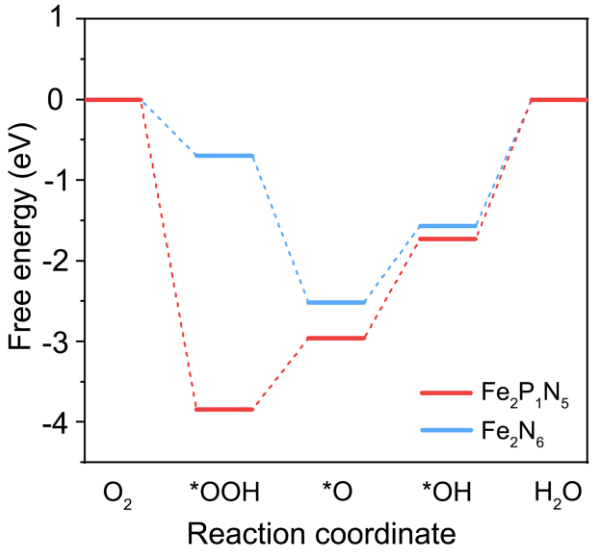

Fig. S71. Free energy diagrams of ORR process on $Fe_2P_1N_5$ and Fe_2N_6.

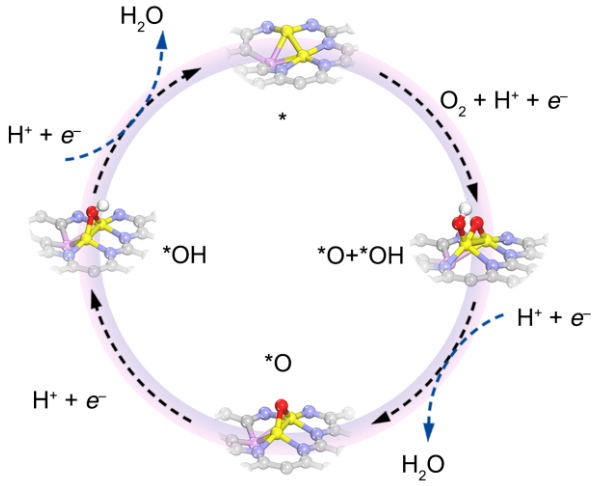

Fig. S72. Optimized configurations of oxygen intermediates adsorbed on $Fe_2P_1N_5$.

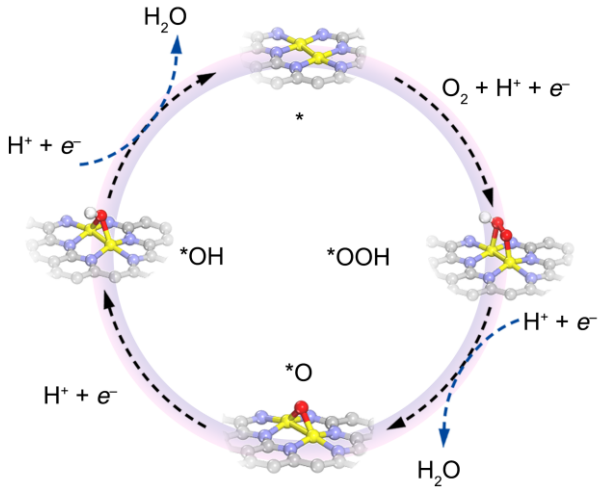

Fig. S73. Optimized configurations of oxygen intermediates adsorbed on Fe_2N_6.

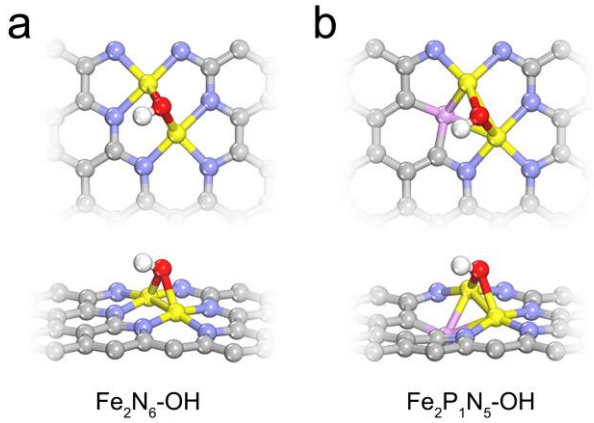

Fig. S74. Optimized atomic structures of (a) Fe_2N_6-OH and (b) $Fe_2P_1N_5$-OH.

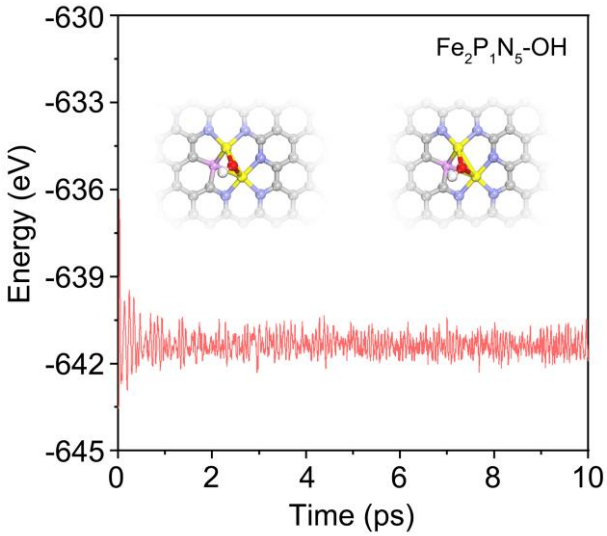

Fig. S75. Energy evolution of $Fe_2P_1N_5$-OH during 10 ps AIMD simulations at 298 K. The inset presents snapshots of the corresponding configurations at the initial and final stages of the AIMD simulations.

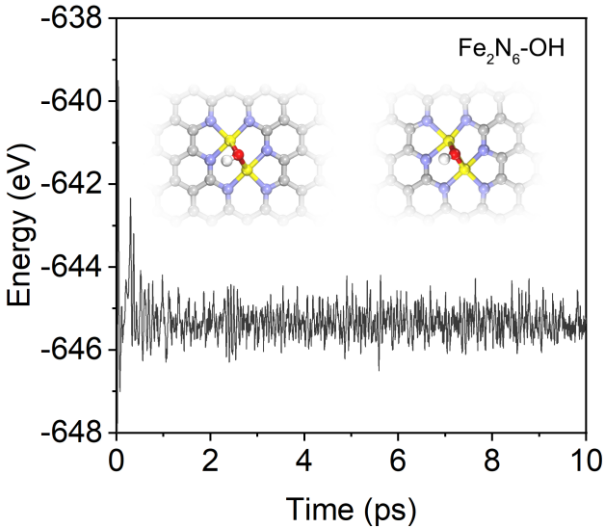

Fig. S76. Energy evolution of Fe_2N_6-OH during 10 ps AIMD simulations at 298 K. The inset presents snapshots of the corresponding configurations at the initial and final stages of the AIMD simulations.

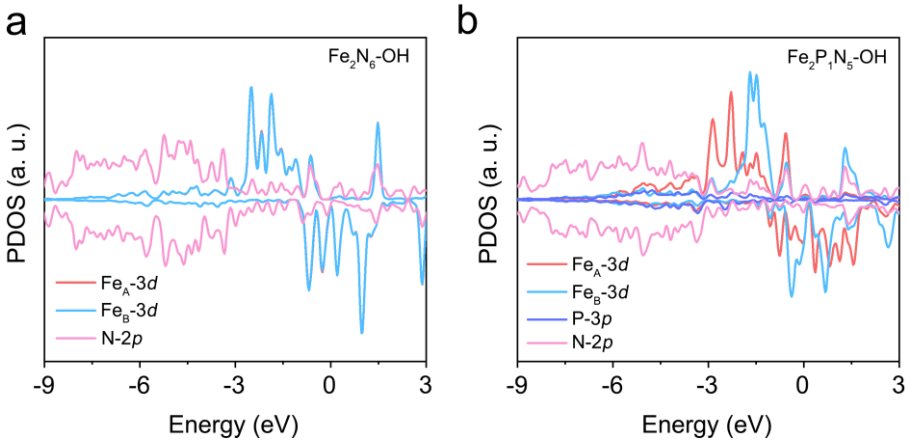

Fig. S77. PDOS diagrams of (a) Fe_2N_6-OH and (b) $Fe_2P_1N_5$-OH.

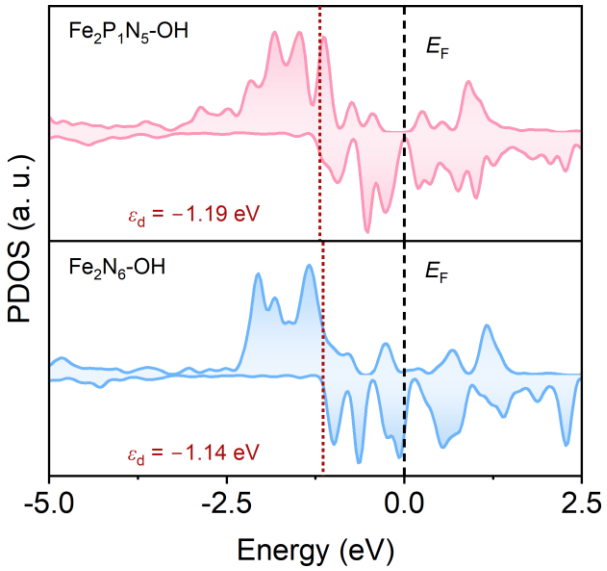

Fig. S78. PDOS of Fe in $Fe_2P_1N_5$-OH and Fe_2N_6-OH and the corresponding *d* band centers.

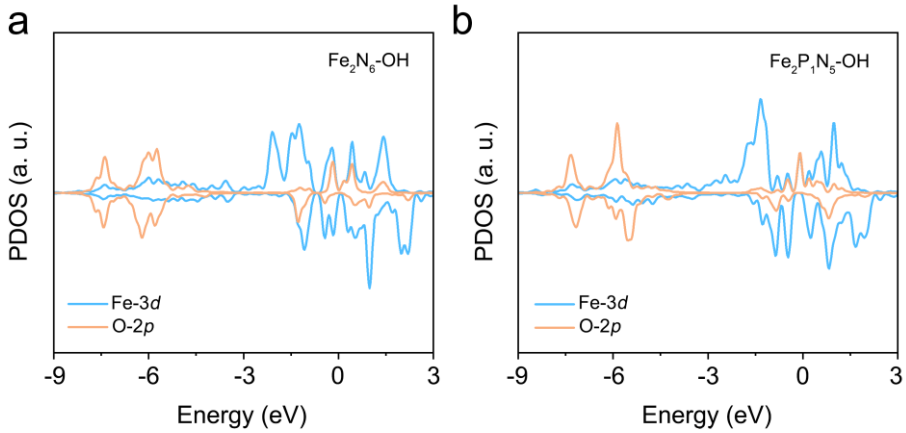

Fig. S79. PDOS diagrams of O_2 activation on (a) Fe_2N_6-OH and (b) $Fe_2P_1N_5$-OH.

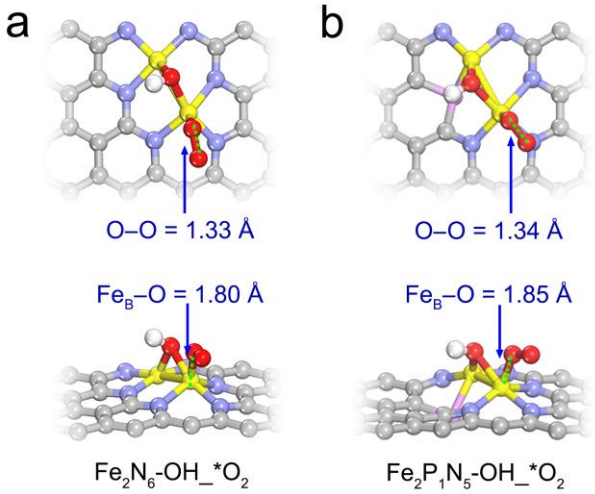

Fig. S80. Optimized structures of *O_2 adsorbed on (a) Fe_2N_6-OH and (b) $Fe_2P_1N_5$-OH.

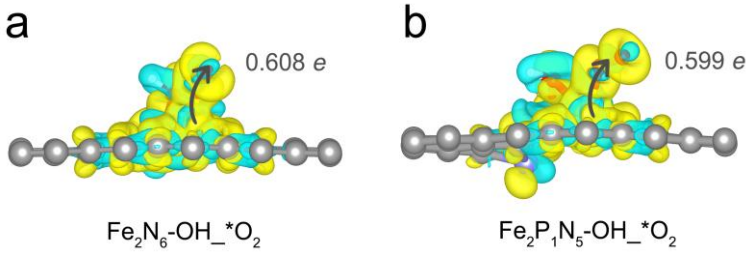

Fig. S81. Differential charge density and Bader charge of *O_2 adsorbed on (a) Fe_2N_6-OH and (b) $Fe_2P_1N_5$-OH. The isosurface value is 0.003 eÅ^{-3}.

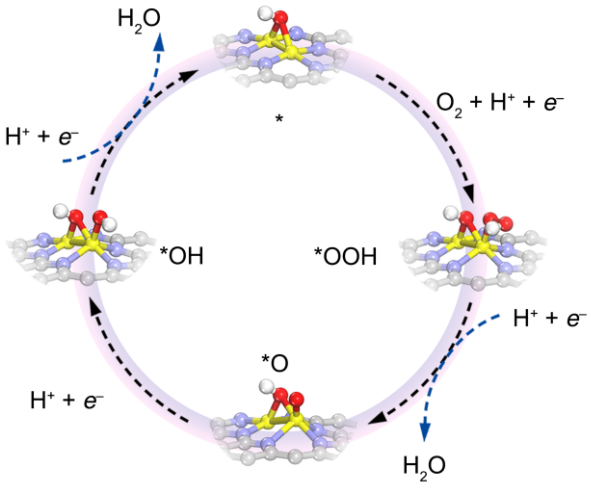

Fig. S82. Optimized configurations of oxygen intermediates adsorbed on Fe_2N_6-OH.

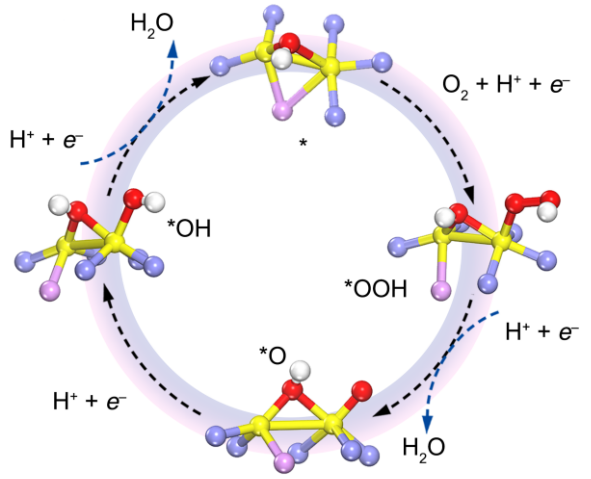

Fig. S83. Optimized configurations of oxygen intermediates adsorbed on $Fe_2P_1N_5$-OH.

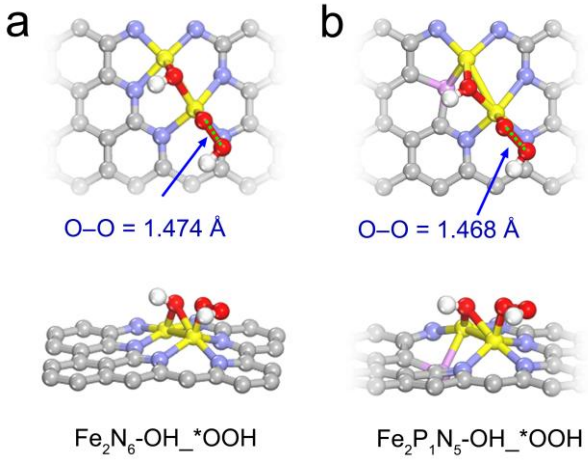

Fig. S84. Optimized structures of *OOH adsorbed on (a) Fe_2N_6-OH and (b) $Fe_2P_1N_5$-OH.

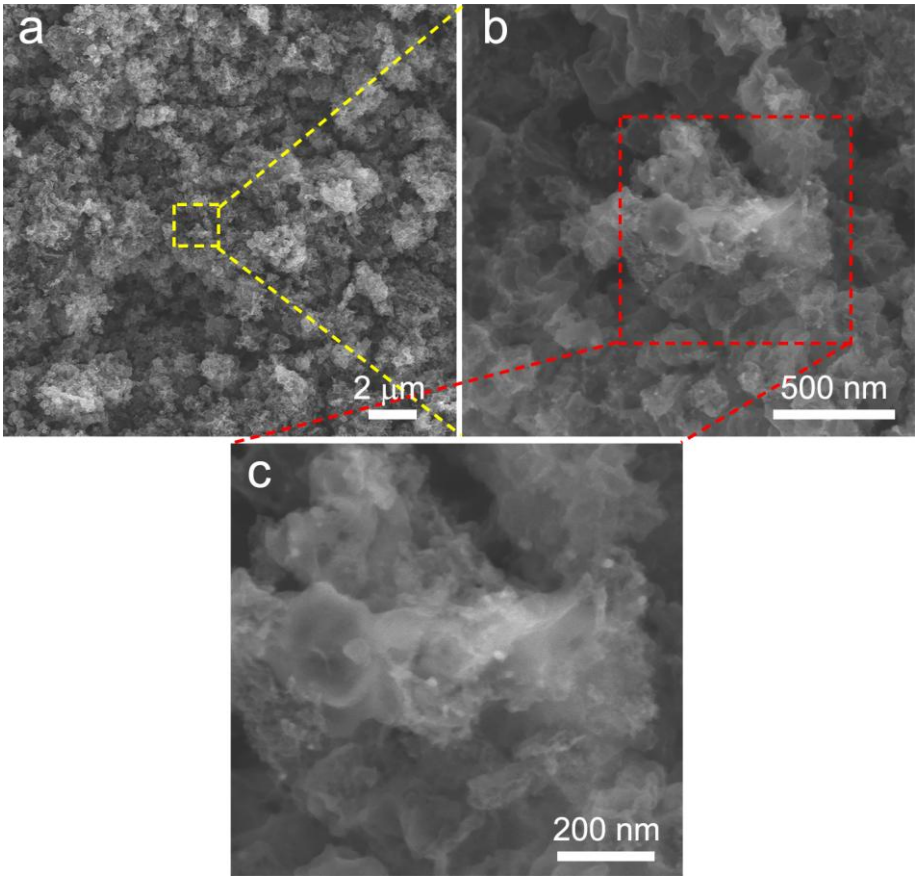

Fig. S85. Morphology characterization of Fe_2/NCP-based zinc-air battery after 550 h charge-discharge cycling tests. (a) SEM image and (b, c) the corresponding enlarged images.

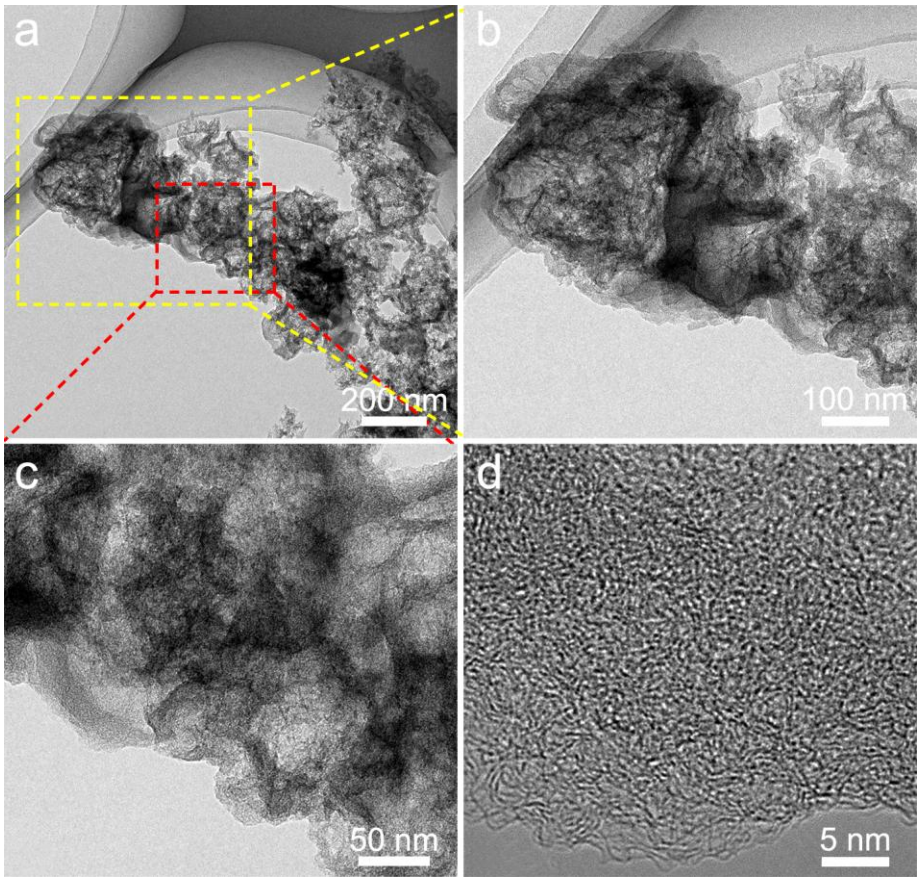

Fig. S86. Morphology characterization of Fe_2/NCP-based zinc-air battery after 550 h charge-discharge cycling tests. (a) TEM image and (b, c) the corresponding enlarged images. (d) HR-TEM image.

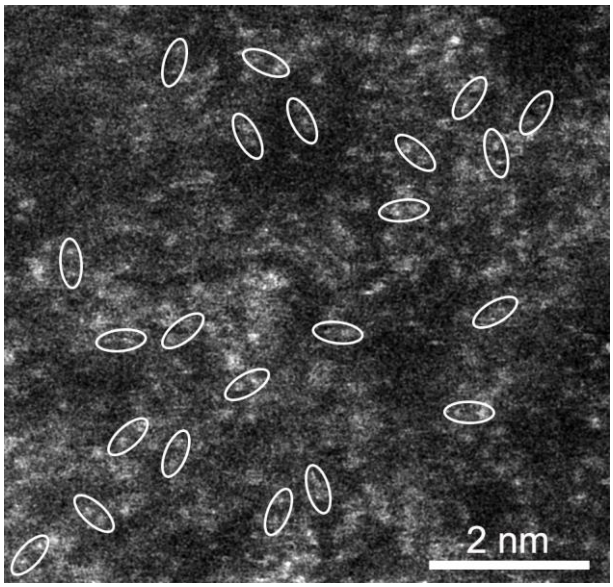

Fig. S87. AC HAADF-STEM image of Fe_2/NCP-based zinc-air battery after 550 h charge-discharge cycling tests.

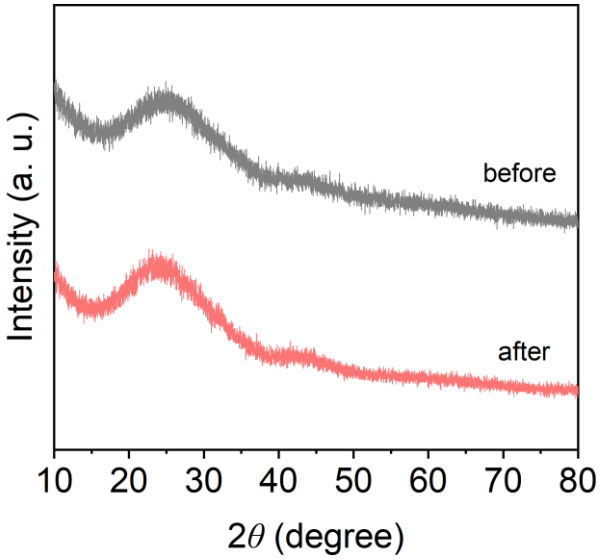

Fig. S88. XRD patterns of Fe_2/NCP-based zinc-air battery before and after 550 h charge-discharge cycling tests.

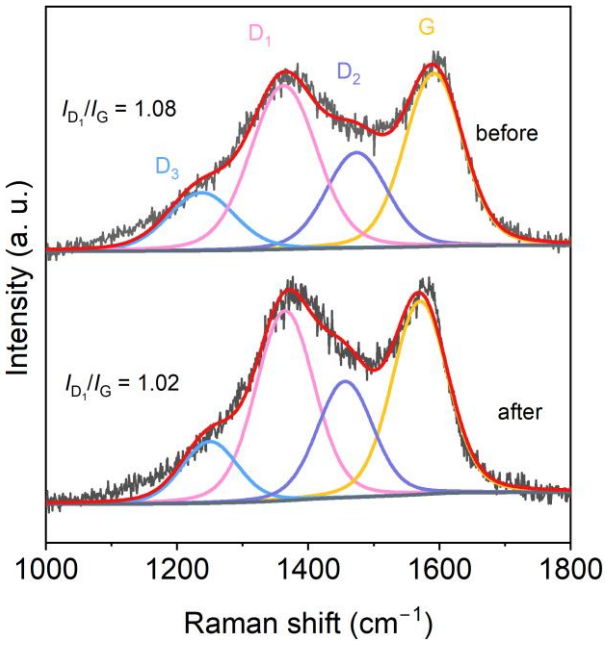

Fig. S89. Raman spectra of Fe_2/NCP-based zinc-air battery before and after 550 h charge-discharge cycling tests.

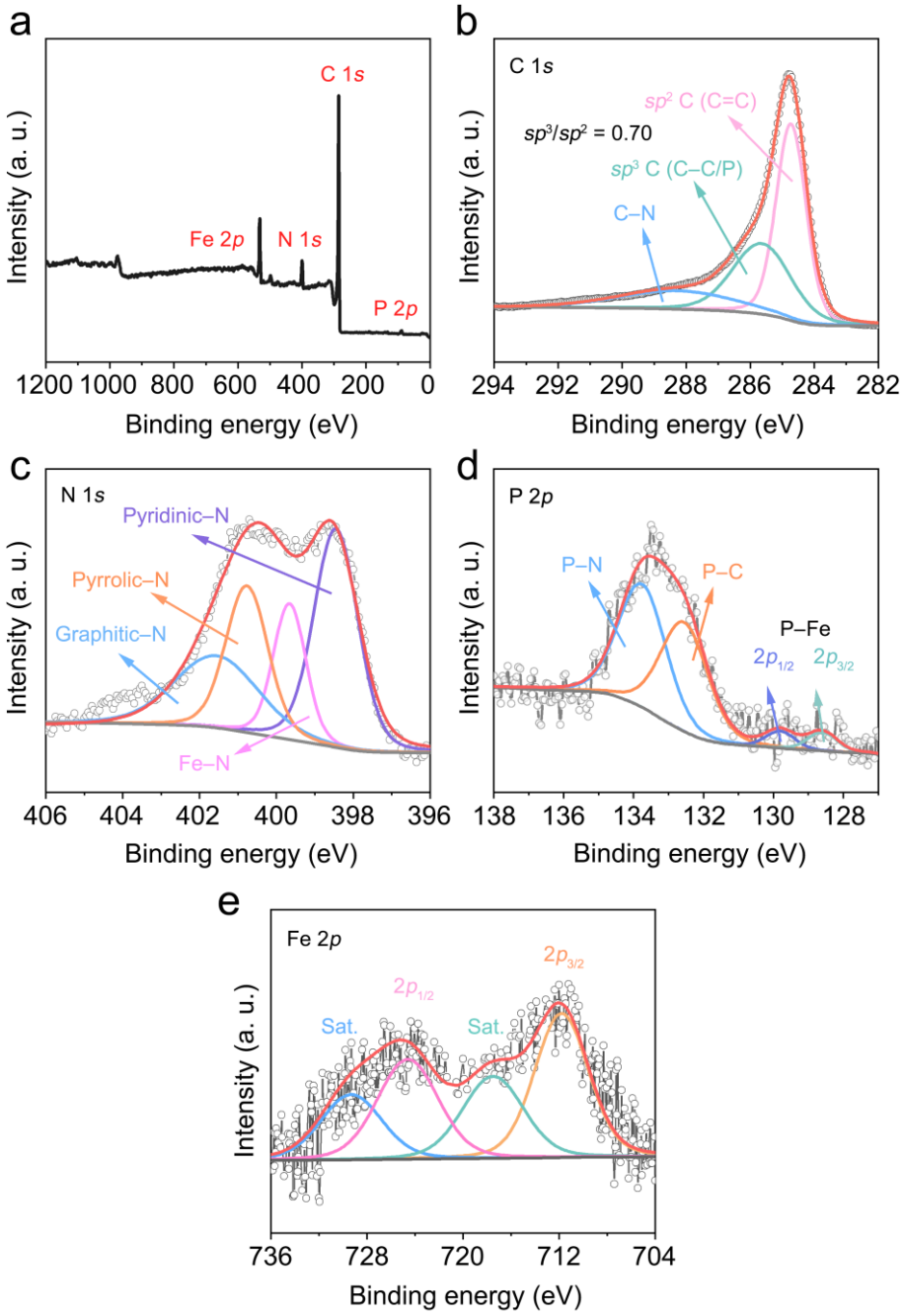

Fig. S90. XPS characterization of Fe_2/NCP-based zinc-air battery after 550 h charge-discharge cycling tests. (a) XPS survey scan, (b) C 1*s*, (c) N 1*s*, (d) P 2*p*, and (e) Fe 2*p* spectra.

Table S1. Fe contents in Fe_2/NCP, Fe_2/NC, and Fe_1/NC determined by ICP-OES.

Sample	Fe (wt%)
Fe_2/NCP	1.33
Fe_2/NC	1.30
Fe_1/NC	0.65

Table S2. Physical properties of samples.

Sample	BET surface area (m^2 g^{-1})	Micropore surface area (m^2 g^{-1})	External surface area (m^2 g^{-1})	Total pore volume (cm^3 g^{-1})
Fe_2/NCP	882.5	376.5	506.0	1.17
Fe_2/NC	847.9	439.6	408.3	0.98
Fe_1/NC	815.1	353.5	461.6	1.07
NCP	695.8	331.2	364.6	0.89
NC	677.6	356.4	321.2	0.88

Table S3. Relative ratios of the deconvoluted C species from C 1*s* spectra of samples.

Sample	sp^2 C (C=C) (%)	sp^3 C (C–C/P) (%)	C–N (%)
Fe_2/NCP	48.89	34.59	16.52
Fe_2/NC	47.46	29.90	22.64
Fe_1/NC	55.01	24.72	20.27

Table S4. Relative ratios of the deconvoluted N species from N 1*s* spectra of samples.

Sample	Pyridinic–N (%)	Pyrrolic–N (%)	Graphitic–N (%)	Fe–N (%)
Fe_2/NCP	36.21	28.98	21.45	13.36
Fe_2/NC	33.47	27.86	25.19	13.48
Fe_1/NC	36.51	34.51	17.42	11.56

Table S5. Structural parameters extracted from the Fe K-edge EXAFS fitting of Fe_2/NCP. (S_0^2=0.85)

Sample	Path	CN	R (Å)	σ^2 (10^{-3} Å^2)	ΔE_0 (eV)	R factor
Fe foil	Fe–Fe	12*	2.48	4.7	5.8	0.004
Fe_2/NCP	Fe–P	0.5	1.95	5.5	4.2	0.009
	Fe–N	2.1	1.86	6.8		
	Fe–Fe	0.8	2.45	5.8		

S_0^2 is the amplitude reduction factor; CN is the coordination number; R is interatomic distance (the bond length between central atoms and surrounding coordination atoms); σ^2 is Debye-Waller factor (a measure of thermal and static disorder in absorber-scatterer distances); ΔE_0 is edge energy shift (the difference between the zero kinetic energy value of the sample and that of the theoretical model). R factor is used to value the goodness of the fitting.

* This value was fixed during EXAFS fitting, based on the known structure. Error bounds that characterize the structural parameters obtained by EXAFS spectroscopy were estimated as N ± 20%; R ± 1%; σ^2 ± 20%; ΔE_0 ± 20%.

Table S6. Comparison of ORR performance of Fe_2/NCP with other previously reported non-precious metal electrocatalysts in 0.1 M KOH.

Catalyst	E_{onset} (V vs. RHE)	$E_{1/2}$ (V vs. RHE)	Tafel slope (mV dec^{-1})	Reference
Fe_2/NCP	**1.08**	**0.94**	**69.8**	**This work**
Fe_2/NC	**1.03**	**0.90**	**73.6**	**This work**
Fe_1/NC	**1.02**	**0.87**	**67.8**	**This work**
NCP	**0.95**	**0.81**	**75.4**	**This work**
NC	**0.94**	**0.79**	**86.4**	**This work**
Pt/C	**1.02**	**0.86**	**73.0**	**This work**
SeFe–C_2N	1.06	0.926	72.0	*Nat. Commun.* **16**, 470 (2025).
MnO_2/Co_2P@SDHC	0.965	0.874	52.44	*Adv. Energy Mater.* **15**, 2405594 (2025).
La_2-NG	0.973	0.893	39	*Angew. Chem. Int. Ed.* **64**, e202509063 (2025).
FeCu-NC	1.03	0.918	—	*Energy Environ. Sci.* **18**, 7624−7634 (2025).
Fe_2BiN_5/C	1.142	0.918	58	*ACS Nano* **19**, 17863−17873 (2025).
Fe_{SA}/Fe_{AC}@PPy/CC	0.97	0.83	75.0	*Energy Environ. Sci.* **18**, 2839–2851 (2025).
SbN_4Cl/NC	1.03	0.921	56	*J. Am. Chem. Soc.* **147**, 21231−21240 (2025).
FeCo–N–C-1.25	1.070	0.853	41.75	*Angew. Chem. Int. Ed.* **64**, e202419595 (2025).
DiFe-N/CBs	1.03	0.917	63.2	*Angew. Chem. Int. Ed.* **64**, e202413933 (2025).
FeOCo-SAD	1.07	0.87	55	*PNAS* **121**, e2404013121 (2024).
Co_{NP}/CoN_2-C	0.99	0.89	56.4	*Adv. Funct. Mater.* **34**, 2410373 (2024).
Fe_xN-NC	0.997	0.873	90.0	*Adv. Energy Mater.* **14**, 2400183 (2024).
CoN_5/PCNF	1.050	0.92	51.2	*Angew. Chem. Int. Ed.* **64**, e202413369 (2024).
Cu-S_1N_3/Cu_x	1.04	0.90	59	*Adv. Funct. Mater.* **33**, 2214425 (2023).
$Co(CN)_3$-Cub	0.99	0.90	57	*Nat. Catal.* **6**, 1164−1173 (2023).

Table S7. Kinetic current densities (J_k) of samples at different potentials in 0.1 M KOH.

Sample	J_k @ 0.80 V (mA cm^{-2})	J_k @ 0.85 V (mA cm^{-2})	J_k @ 0.90 V (mA cm^{-2})
Fe_2/NCP	56.92	37.46	12.79
Fe_2/NC	45.75	16.05	6.27
Fe_1/NC	21.97	5.34	1.36
NCP	5.82	1.56	0.34
NC	3.92	1.16	0.30
Pt/C	15.95	6.31	1.95

Table S8. Mass activity of samples at different potentials in 0.1 M KOH.

Sample	MA @ 0.80 V (10^3 A g^{-1})	MA @ 0.85 V (10^3 A g^{-1})	MA @ 0.90 V (10^3 A g^{-1})
Fe_2/NCP	18.64	12.27	4.19
Fe_2/NC	15.33	5.38	2.10
Fe_1/NC	14.72	3.58	0.91
Pt/C	0.35	0.14	0.04

Table S9. TOF of samples at different potentials in 0.1 M KOH.

Sample	TOF @ 0.80 V (s^{-1})	TOF @ 0.85 V (s^{-1})	TOF @ 0.90 V (s^{-1})
Fe_2/NCP	10.77	7.09	2.42
Fe_2/NC	8.86	3.11	1.21
Fe_1/NC	8.51	2.07	0.53
Pt/C	0.70	0.28	0.09

Table S10. Relative ratios of the deconvoluted N species from N 1*s* spectra of Fe_2/NCP before and after 40000 potential cycles in 0.1 M KOH.

Sample	Pyridinic–N (%)	Pyrrolic–N (%)	Graphitic–N (%)	Fe–N (%)
before	36.21	28.98	21.45	13.36
after	38.70	26.28	22.05	12.97

Table S11. Relative ratios of the deconvoluted C species from C 1*s* spectra of Fe_2/NCP before and after 40000 potential cycles in 0.1 M KOH.

Sample	sp^2 C (C=C) (%)	sp^3 C (C–C/P) (%)	C–N (%)
before	48.89	34.59	16.52
after	49.88	34.71	15.41

Table S12. Relative ratios of the deconvoluted P species from P 2*p* spectra of Fe_2/NCP before and after 40000 potential cycles in 0.1 M KOH.

Sample	P–N (%)	P–C (%)	P–Fe (%)
before	38.75	57.87	3.38
after	50.34	44.23	5.43

Table S13. The equivalent circuits fitting results of Fe_2/NCP at different potentials in 0.1 M KOH.

Potential (V vs. RHE)	R_s	R_{ct}	C_{dl}	R_{mt}	C_{rxn}
1.15	37.8	73.74	0.017839	2.79	0.050569
1.10	37.85	63.33	0.017352	2.178	0.055932
1.05	37.89	50.88	0.016261	1.971	0.056127
1.00	37.94	32.61	0.014465	1.931	0.011544
0.95	37.98	23.43	0.0144	1.621	0.052073
0.90	38.01	15.71	0.013092	1.433	0.0036098
0.85	37.96	33.17	0.024661	1.226	0.032344
0.80	37.9	57.88	0.026602	0.80209	0.025087
0.75	37.78	70.55	0.0224602	0.50532	0.050569

Table S14. The equivalent circuits fitting results of Fe_2/NC at different potentials in 0.1 M KOH.

Potential (V vs. RHE)	R_s	R_{ct}	C_{dl}	R_{mt}	C_{rxn}
1.10	38.08	156.79	0.012664	4.804	0.026005
1.06	38.08	135.9	0.012411	4.342	0.024954
1.02	38.07	111.38	0.012015	3.808	0.015453
0.98	38.11	105.72	0.056398	3.569	0.013269
0.94	38.19	92.94	0.011021	2.676	0.01173
0.90	38.3	78.52	0.014461	2.075	0.0084272
0.86	39.1	55.41	0.0108	1.913	0.0051306
0.82	38.95	79.46	0.014624	1.836	0.0038908
0.78	38.99	108.45	0.01894	1.712	0.010242
0.74	38.82	137.9	0.020311	1.22	0.026005

Table S15. The equivalent circuits fitting results of Fe_1/NC at different potentials in 0.1 M KOH.

Potential (V vs. RHE)	R_s	R_{ct}	C_{dl}	R_{mt}	C_{rxn}
1.05	38.26	175.7	0.005942	6.997	0.0068254
1.01	38.11	136.7	0.00762	5.737	0.0049194
0.97	38.24	111.8	0.0067648	4.829	0.0058039
0.93	38.29	109.5	0.0076014	4.732	0.0051145
0.89	38.42	93.26	0.0062827	4.48	0.0028333
0.85	38.46	79.21	0.0076227	4.249	0.00097911
0.81	38.21	93.69	0.01333	3.94	0.0010625
0.77	38.03	141.61	0.014497	3.213	0.0097835
0.73	38.15	167	0.015876	2.449	0.0070438
0.69	38.12	267.9	0.01404	1.51	0.0063246

Table S16. Comparison of ORR performance of Fe_2/NCP with other previously reported non-precious metal electrocatalysts in 0.5 M H_2SO_4.

Catalyst	E_{onset} (V vs. RHE)	$E_{1/2}$ (V vs. RHE)	Tafel slope (mV dec^{-1})	Reference
Fe_2/NCP	**0.93**	**0.82**	**73.8**	**This work**
Fe_2/NC	**0.85**	**0.73**	**86.7**	**This work**
Fe_1/NC	**0.86**	**0.67**	**107.9**	**This work**
NCP	**0.83**	**0.64**	**112.6**	**This work**
NC	**0.80**	**0.51**	**177.7**	**This work**
Pt/C	**0.97**	**0.84**	**70.9**	**This work**
T-FeCo-N-C	—	0.818	86.95	*Nat. Commun.* **16**, 7198 (2025).
CA-Fe@BC	0.86	0.78	64.1	*Nat. Commun.* **16**, 2920 (2025).
Fe_1-N_4SO_2/NC ($HClO_4$)	—	0.772	55	*J. Am. Chem. Soc.* **147**, 6914−6924 (2025).
CuFeDAC-NC ($HClO_4$)	—	0.811	37.55	*Adv. Funct. Mater*. **35**, 2503079 (2025).
FeN_5-NHC ($HClO_4$)	0.98	0.85	89.4	*Angew. Chem. Int. Ed.* **64**, e202505937 (2025).
Zn-N-P/NPC ($HClO_4$)	0.93	0.80	48.3	*Adv. Mater.* **37**, 2503254 (2025).
Ru,Fe-NC DAS ($HClO_4$)	—	0.843	76	*Energy Environ. Sci.* **17**, 3077–3087 (2024).
FeNS/Fe_3C@CNS ($HClO_4$)	0.90	0.78	106	*Angew. Chem. Int. Ed.* **63**, e202313034 (2024).
Fe_2–S_1N_5/SNC ($HClO_4$)	0.929	0.829	51	*Energy Environ. Sci.* **17**, 4646–4657 (2024).
Fe_3C-Fe_1/CNT	0.93	0.83	75.9	*Natl. Sci. Rev.* **11**, nwae193 (2024).
Fe-SA/PNC	0.988	0.842	70	*Angew. Chem. Int. Ed.* **62**, e202307504 (2023).
Fe-Zn@SNC	0.99	0.86	64	*Angew. Chem. Int. Ed.* **62**, e202301833 (2023).
$FeMn_{ac}$/Mn-N_4C	0.89	0.79	108.5	*Angew. Chem. Int. Ed.* **62**, e202214988 (2023).
FePCN	0.88	0.76	59.7	*Adv. Energy Mater.* **13**, 2301223 (2023).

Table S17. Kinetic current densities (J_k) of samples at different potentials in 0.5 M H_2SO_4.

Sample	J_k @ 0.80 V (mA cm^{-2})	J_k @ 0.85 V (mA cm^{-2})	J_k @ 0.90 V (mA cm^{-2})
Fe_2/NCP	9.85	2.19	0.38
Fe_2/NC	1.05	0.37	0.08
Fe_1/NC	0.42	0.12	0.04
NCP	0.20	0.08	0.03
NC	0.10	0.06	0.04
Pt/C	13.51	3.92	1.00

Table S18. Mass activity of samples at different potentials in 0.5 M H_2SO_4.

Sample	MA @ 0.80 V (10^3 A g^{-1})	MA @ 0.85 V (10^3 A g^{-1})	MA @ 0.90 V (10^3 A g^{-1})
Fe_2/NCP	3.23	0.727	0.124
Fe_2/NC	0.35	0.124	0.027
Fe_1/NC	0.28	0.080	0.027
Pt/C	0.29	0.085	0.022

Table S19. TOF of samples at different potentials in 0.5 M H_2SO_4.

Sample	TOF @ 0.80 V (s^{-1})	TOF @ 0.85 V (s^{-1})	TOF @ 0.90 V (s^{-1})
Fe_2/NCP	1.86	0.414	0.072
Fe_2/NC	0.20	0.072	0.015
Fe_1/NC	0.16	0.046	0.015
Pt/C	0.59	0.172	0.044

Table S20. Relative ratios of the deconvoluted N species from N 1*s* spectra of Fe_2/NCP before and after 40000 potential cycles in 0.5 M H_2SO_4.

Sample	Pyridinic−N (%)	Pyrrolic−N (%)	Graphitic−N (%)	Fe−N (%)
before	36.21	28.98	21.45	13.36
after	35.33	26.59	24.23	13.85

Table S21. Relative ratios of the deconvoluted C species from C 1*s* spectra of Fe_2/NCP before and after 40000 potential cycles in 0.5 M H_2SO_4.

Sample	sp^2 C (C=C) (%)	sp^3 C (C−C/P) (%)	C−N (%)
before	48.89	34.59	16.52
after	51.29	35.22	13.49

Table S22. Relative ratios of the deconvoluted P species from P 2*p* spectra of Fe_2/NCP before and after 40000 potential cycles in 0.5 M H_2SO_4.

Sample	P−N (%)	P−C (%)	P−Fe (%)
before	38.76	57.87	3.37
after	60.59	37.71	1.70

Table S23. The equivalent circuits fitting results of Fe_2/NCP at different potentials in 0.5 M H_2SO_4.

Potential (V vs. RHE)	R_s	R_{ct}	C_{dl}	R_{mt}	C_{rxn}
1.00	4.857	385.75	0.013317	7.677	0.076598
0.95	4.616	342.29	0.012927	6.167	0.053032
0.90	4.693	195.6	0.012364	2.682	0.019395
0.85	4.644	162.9	0.011306	2.578	0.041904
0.80	4.689	111.8	0.01469	1.532	0.018234
0.75	4.716	124.2	0.012664	0.77333	0.01496
0.70	4.653	241.9	0.015407	0.56581	0.006452
0.65	4.675	256.6	0.011043	0.53483	0.012492

Table S24. The equivalent circuits fitting results of Fe_2/NC at different potentials in 0.5 M H_2SO_4.

Potential (V vs. RHE)	R_s	R_{ct}	C_{dl}	R_{mt}	C_{rxn}
0.95	5.382	4778	0.0021004	8.047	0.051481
0.90	5.352	1004	0.0021461	6.309	0.026288
0.85	5.269	544	0.0023031	4.024	0.017034
0.80	5.273	353.9	0.0027365	2.423	0.017968
0.75	5.35	351.1	0.0033863	2.206	0.0082054
0.70	5.391	412.6	0.0036771	1.429	0.005566
0.65	5.388	509.8	0.0035979	1.252	0.0042431
0.60	5.357	764	0.0034017	1.637	0.0032626
0.55	5.267	970.8	0.0031996	1.047	0.0094711

Table S25. The equivalent circuits fitting results of Fe_1/NC at different potentials in 0.5 M H_2SO_4.

Potential (V vs. RHE)	R_s	R_{ct}	C_{dl}	R_{mt}	C_{rxn}
0.95	6.885	8258	0.001973	10.05	0.0075845
0.90	7.009	2494	0.0020625	6.835	0.0074355
0.85	6.978	1086	0.0021515	6.507	0.0069616
0.80	7.063	750.2	0.002305	6.785	0.0072531
0.75	6.926	614	0.002704	4.798	0.0049437
0.70	6.962	576.6	0.0030274	4.035	0.0041211
0.65	6.87	634.6	0.0032529	3.345	0.0033875
0.60	6.884	1051	0.0033229	3.045	0.0029116
0.55	6.875	1538	0.0034589	2.823	0.0012966

Table S26. Zero-point energy (E_{ZPE}) and entropy contribution (TS) of the reaction intermediates.

Species	E_{ZPE} **(eV)**	TS **(eV)**
$*O_2$	0.14	0.15
*OOH	0.44	0.18
*O	0.07	0.07
*OH	0.35	0.10

Table S27. Comparison of Zn-air battery performance between Fe_2/NCP and other previously reported non-precious metal electrocatalysts.

Catalyst	OCP (V)	Peak power density (mW cm^{-2})	Specific capacity (mAh g^{-1})	Reference
Fe_2/NCP	**1.58**	**300.4**	**733.8 (20 mA cm^{-2})**	**This work**
Fe_2/NC	**1.54**	**230.5**	**688.1 (20 mA cm^{-2})**	**This work**
Fe_1/NC	**1.48**	**204.1**	**647.6 (20 mA cm^{-2})**	**This work**
Pt/C+RuO_2	**1.43**	**109.4**	**617.0 (20 mA cm^{-2})**	**This work**
CoCo-BiSalphen@KB	1.512	215.7	800.6 (100 mA cm^{-2})	*Nat. Commun.* **16**, 921 (2025).
SbN_4Cl/NC	1.49	193	793 (15 mA cm^{-2})	*J. Am. Chem. Soc.* **147**, 21231−21240 (2025).
Co-N-Mn/NC	1.51	271	805(10 mA cm^{-2})	*Nat. Commun.* **16**, 5158 (2025).
CoMn−NSC	1.56	152.2	—	*Adv. Funct. Mater.* **35**, 2504260 (2025).
FeCu-NC	1.53	250.3	787 (20 mA cm^{-2})	*Energy Environ. Sci.* **18**, 7624–7634 (2025).
Co_3-NG	1.48	189.0	770.3 (10 mA cm^{-2})	*Angew. Chem. Int. Ed*. **64**, e202503019 (2025).
Co-FNC	1.55	246	817 (10 mA cm^{-2})	*ACS Nano* **18**, 11474–11486 (2024).
CR-Co/ClNC	1.50	176.6	745 (10 mA cm^{-2})	*Nat. Commun.* **15**, 1675 (2024).
ZnCoFe-TAC/SNC	1.40	304	760 (5 mA cm^{-2})	*Energy Environ. Sci.* **17**, 2298–2308 (2024).
FeCo-SAs	1.475	203.36	805.46 (10 mA cm^{-2})	*ACS Nano* **18**, 13006−13018 (2024).
$Fe_{SAs+NPs}Ce_{SAs+Fe-ONPs}$/NC	1.55	240.5	788.2 (10 mA cm^{-2})	*Angew. Chem. Int. Ed.* **63**, e202400765 (2024).
c-$CoSe_2$-CoN/NC	1.52	118	802 (10 mA cm^{-2})	*Adv. Mater.* **36**, 2306844 (2024).
FeCo-*D*SA/AC	1.489	174.1	793.30 (10 mA cm^{-2})	*Angew. Chem. Int. Ed.* **63**, e202412566 (2024).
FeCo–N_3O_3@C	1.43	143	787.2 (10 mA cm^{-2})	*Nat. Synth.* **3**, 878–890 (2024).
Fe_2-pPc	1.446	255	791 (10 mA cm^{-2})	*J. Am. Chem. Soc.* **146**, 24842−24854 (2024).

Table S28. Relative ratios of the deconvoluted N species from N 1*s* spectra of Fe_2/NCP-based zinc-air battery before and after 550 h charge-discharge cycling tests.

Sample	Pyridinic–N (%)	Pyrrolic–N (%)	Graphitic–N (%)	Fe–N (%)
before	36.21	28.98	21.45	13.36
after	36.86	26.02	19.35	17.77

Table S29. Relative ratios of the deconvoluted C species from C 1*s* spectra of Fe_2/NCP-based zinc-air battery before and after 550 h charge-discharge cycling tests.

Sample	sp^2 C (C=C) (%)	sp^3 C (C–C/P) (%)	C–N (%)
before	48.89	34.59	16.52
after	48.31	33.81	17.88

Table S30. Relative ratios of the deconvoluted P species from P 2*p* spectra of Fe_2/NCP-based zinc-air battery before and after 550 h charge-discharge cycling tests.

Sample	P–N (%)	P–C (%)	P–Fe (%)
before	38.75	57.87	3.38
after	48.39	42.86	8.75

Table S31. Comparison of the performance of flexible quasi-solid-state zinc-air batteries powered by Fe_2/NCP versus other reported non-precious metal electrocatalysts.

Catalyst	GPEs	OCP (V)	Peak power density (mW cm^{-2})	Reference
Fe_2/NCP	**PVA**	**1.40**	**166.9**	**This work**
Fe_2/NC	**PVA**	**1.37**	**136.0**	**This work**
Fe_1/NC	**PVA**	**1.32**	**114.1**	**This work**
Pt/C+RuO_2	**PVA**	**1.26**	**70.4**	**This work**
Fe-SAs/MPC	PVA	1.47	198	*Angew. Chem. Int. Ed.* **64**, e202501307 (2025).
Co_{AC}-Mo_xC/CC	PAA	1.47	103.4	*Adv. Funct. Mater.* **35**, 2506077 (2025).
MnO_2/Co_2P@SDHC	PAM	1.47	75	*Adv. Energy Mater.* **15**, 2405594 (2025).
Fe-N_4/N_{GC}-C	PANa	1.43	136	*Natl. Sci. Rev.* **12**, nwaf061 (2025).
$NiCo_2S_4$@NiFe LDH/N-rGO	PAA	1.44	111	*Energy Environ. Sci.* **18**, 991−1001 (2025).
SA-Cu@NCA	PVA	1.42	98.5	*ACS Nano* **19**, 23859−23868 (2025).
Fe_x/FeN_3S_1–C	CNF@PVA-SSE	1.46	96.54	*Energy Environ. Sci.* **17**, 4746–4757 (2024).
$NiCo_{1.8}Fe_{0.2}O_4$@NCF	PVA	1.46	80	*Angew. Chem. Int. Ed.* **63**, e202319983 (2024).
CoFe/AC	PAM-SC	1.37	107.64	*Angew. Chem. Int. Ed.* **62**, e202301114 (2023).
Co_9S_8-NSABP	PANa–PVA–IL	1.475	198	*Adv. Mater.* **35**, 2209980 (2023).
Fe_3Co_7-NC	PAA	1.51	133	*Adv. Funct. Mater.* **33**, 2212299 (2023).
Nd/Co@NC	PAA	1.36	70.6	*Adv. Energy Mater.* **13**, 2203244 (2023).